Ben-Gurion University of the Negev

The Faculty of Engineering Sciences

The Department of Mechanical Engineering

Numerical simulation of three-dimensional eletro-thermobuoyant flows in enclosure

Thesis submitted in partial fulfillment of the requirements

for the Master of Sciences degree

Yohay Mayan

Under the supervision of **Dr. Yuri Feldman**

March 2023

Ben-Gurion University of the Nagev
The Faculty of Engineering Sciences
Department of Mechanical Engineering

Numerical simulation of three-dimensional eletro-thermobuoyant flows in enclosure

A thesis submitted
in partial fulfillment of the requirements
for the Degree of

Master of Sciences
in
Mechanical Engineering
by

Yohay Mayan

Under the supervision of: **Dr. Yuri Feldman**

Signature of student: _____ **Date:** 21.03.2023
Signature of supervisor: Feldman **Date:** 21.03.2023
Signature of chairperson of the committee for graduate studies: _____ **Date:** 21/3/23

ד"ר בני בר-און
יו"ר לימודי מוסמכים
המחלקה להנדסת מכונות

ACKNOWLEDGEMENTS

Completing this thesis has been made possible through the invaluable support and assistance of several individuals and organizations, to whom I express my sincere gratitude. First and foremost, I am deeply indebted to my supervisor, Dr. Yuri Feldman, for his professional and knowledgeable guidance in the physical, computational, and numerical fields. His significant contribution to this research, from his laboratory computing equipment to countless hours of meetings and advice at any time, has been remarkable. I am incredibly grateful for his meticulous supervision while writing this scientific manuscript. The Council for Higher Education, through the Hamer scholarship, together with the Ben-Gurion Faculty of Mechanical Engineering scholarship, provided the necessary financial support for this research. I am grateful for their invaluable contributions to this work. I would also like to acknowledge my colleagues at the Computational Physics Lab, founded by Dr. Yuri Feldman, for their insightful discussions and technical assistance. Their contributions have been instrumental in the successful completion of this research. In addition, I would like to thank my colleague Dr. Mukesh Kumar for his endless help and patience throughout the writing and editing process. Finally, I thank my family and friends for their unwavering interest and encouragement throughout this academic journey. Their emotional support has been invaluable, and I am forever grateful for their steadfast encouragement.

ABSTRACT

This thesis presents the development of an immersed boundary/finite volume framework for electro-hydrodynamics (EHD) flows with heat transfer. The method discretizes the governing equations using a staggered finite volume framework on Cartesian meshes. The solver employs a standard incremental fractional step approach with three-point backward differencing in time to solve the governing conservation laws, resulting in a nominally second-order accurate solver in space and time. The finite volume solver serves as the basic workhorse for the immersed boundary techniques proposed in the thesis. The thesis proposes a direct forcing immersed boundary approach for electro-hydrodynamics flows with heat transfer. This approach assumes that the forcing function is added to the Navier-Stokes equations, allowing for the construction of modified governing laws that account for both Dirichlet and Neumann boundary conditions. The accuracy of the IB-FV solver has been evaluated for electro-hydrodynamics flows, and it has been found to produce accurate results. The solver is capable of computing the surface-averaged Nusselt number with high accuracy. The idea underlying the direct forcing immersed boundary method is extended to solve electro-thermo-convection problems as well. The resulting solver is capable of tackling electro-thermo-convection problems developing around immersed bodies of an arbitrary shape. A spectrum of test cases performed in the framework of the current study demonstrates the accuracy and efficacy of the IB-FV solver for EHD flows with heat transfer. The numerous test problems presented in this thesis serve to comprehensively evaluate and establish the proposed direct forcing immersed boundary/finite volume framework as a robust, simple, and accurate approach for simulating EHD flows with heat transfer. These test problems demonstrate the effectiveness of the proposed method in simulating various types of flows, including electro-convection and electro-thermo-convection flows, and its ability to accurately compute surface-averaged Nusselt numbers and vortical structure of the flow. The results suggest that the proposed method is a reliable and effective computational tool for studying the EHD flows with heat transfer. As a novel aspect, the

developed solver is used to investigate the potential of electro-convection in enhancement of heat transfer rate from the surface of injecting sphere immersed into perfectly insulating liquid.

CONTENTS

LIST OF FIGURES

NOMENCLATURE

Symbols

Initials	Description	Units
$\mathbf{u}$	Velocity	$\frac{m}{s}$
P	Pressure	$\frac{N}{m^2}$
$\vec{g}$	Gravity acceleration	$\frac{m}{s^2}$
H	cube side length	m
θ	Temperature	K
q	Charge density	$\frac{C}{m^3}$
D	Molecular diffusion coefficient	$\frac{m^2}{s}$
t	Time	s
C_p	Specific heat capacity at constant pressure	$\frac{J}{kgK}$
K	Ionic mobility	$\frac{m^2}{Vs}$
V	Volume	m^3
$\vec{X}^K(X^K, Y^K)$	Coordinates of Lagrangian grid points	m
$\vec{x}_i(x_i, y_j)$	Coordinates on Eulerian grid	m
$f_\psi(\vec{x}_i)$	Immersed forces/sources of ψ field on Eulerian grid points	$[\psi]$
$F_\Psi^K(\vec{X}^K)$	Immersed forces/sources of ψ field on Lagrangian grid points	$[\Psi]$
$\boldsymbol{L}$	Laplace operator	
$\boldsymbol{I}$	Interpolation operator	

Symbols

Initials	Description	Units
$\boldsymbol{R}$	Regularization operator	
$\boldsymbol{H}$	Helmholtz operator	
$\boldsymbol{N}$	Non-linear terms	
$\mathbf{I}$	Unity matrix	
R	Sphere radius	
S	Corresponds to all Lagrangian grid cells	

Subscripts

Symbol	Description	Symbol	Description
0	Characteristic value	h	Hot surface
c	Cold surface	i,j,k	Eulerian grid

Operators

Symbol	Description	Symbol	Description
$\cdot$	Scalar multiplication	$\times$	Vector multiplication
$\left[\quad \right]$	Tensor	$\frac{\partial}{\partial j}$	Derivative by variable j
∇	Gradient	$\nabla\cdot$	Divergence
Δ	Difference	∇^2	Laplacian

Superscripts

Symbol	Description	Symbol	Description
$\tilde{}$	Dimensional value	$\longrightarrow$	Vector
n	Current time step	$n-1$	Previous time step
$n+1$	Next time step	*	Intermediate predicted velocity field
K	Lagrangian grid		

Dimensionless variables

Symbol	Description	Formulation
Ra	Rayleigh number	$\frac{\vec{g}\beta\Delta\theta H^3}{\kappa\nu}$
Pr	Prandtl number	$\frac{\nu}{\alpha_0}$
T	electric Rayleigh number	$\frac{\varepsilon\phi_0}{\rho\nu K}$
Γ	Aspect ratio between inner radius and outer side length	$\frac{R}{H}$
M	Dimensionless ionic mobility number	$\frac{1}{K}\sqrt{\frac{\varepsilon}{\rho}}$
$\hat{D}$	Dimensionless molecular diffusion coefficient	$\frac{D}{\nu}$
C	Injection strength number	$\frac{q_0 H^2}{\varepsilon\phi_0}$

Abbreviations

Sign	Description	Sign	Description
BC	Boundary Condition(s)	IC	Initial Condition(s)
NS	Navier-Stokes	EDF	Electrically-Driven Flow
EHD	ElectroHydroDynamics	PNP	Poisson-Nernst-Planck
DH	Debye-Hückel	PB	Poisson-Boltzmann
SIMPLE	Semi-Implicit Method for Pressure Linked Equations.	PB	Poisson-Boltzmann
RHS	Right Hand Side	IB	Immersed boundary
CFD	Computational fluid dynamics		

Greek Letters

Initials	Description	Units
ϕ	Electric potential	V
ρ	Density	$\frac{kg}{m^3}$
ν	Kinematics viscosity	$\frac{m^2}{s}$
β	Volumetric expansion coefficient	$\frac{1}{K}$
κ	Thermal conductivity	$\frac{W}{m^2K}$
θ	Non-dimensional temperature	$\frac{W}{m^2K}$
α_0	Thermal diffusivity	$\frac{m^2}{s}$
ε	Electrical permittivity	$\frac{F}{m}$
α	The section plane angle	$deg°$
δ	Discrete Dirac function	m
ψ	Eulerian fields	$[\psi]$
Ψ	Lagrangian fields	$[\Psi]$
λ_2	Median eigenvalue	
ω	Frequency of oscillation	$\frac{1}{s}$
Ω	Corresponds to all Eulerian grid cells	
ε_K	Corresponds to all Eulerian grid cells	
ε_K	X coordinate of the Lagrangian point	
η_K	Y coordinate of the Lagrangian point	
ζ_K	Z coordinate of the Lagrangian point	
U^Γ	Boundary velocity	
Φ^Γ	Boundary electric potential	
Q^Γ	Boundary charge density	
Θ^Γ	Boundary temperature	

CHAPTER 1

INTRODUCTION

EHD flows play a significant role in various engineering applications, such as nuclear reactors [1], micro-flow pumps [2, 3], industrial printers [4],and lubrication in bearings [5]. Despite a large volume of experimental studies aimed at understanding the fundamental mechanisms driving the EHD flows and improving the design of specific engineering configurations, conducting experiments is often challenging and prohibitively expansive. Fortunately, the emergence of advanced computing facilities and the development of computational techniques have provided a viable approach to address complex electro-thermo-convection flow problems using robust numerical frameworks. To study the EHD flows coupled with heat transfer relevant to various engineering applications, it is crucial to consider the dominant modes of charge transport, namely : drift and diffusion, and their impact on the flow. In the drift mode, the charge carriers move due to the influence of electric field. When the electric field is applied, it causes the charge carriers to accelerate in the direction of the field. The extent of the drift depends on the strength of the electric field and the mobility of the charge carriers. In the diffusion mode, the charge carriers move due to their thermal motion. In material or device with a concentration gradient of charge carriers, the carriers will diffuse from the high concentration to the low concentrations regions . The interplay between the physical laws governing the fluid dynamics, the charge transport and the heat transfer makes these problems both challenging for numerical approaches and

fascinating from a physical perspective. Problems involving electro-thermo-convection has been extensively studied in literature [6–9] and have been largely simulated in two-dimensional domain. However, practical geometries, are complex and not amenable to simple grid-generation, unlike several canonical problems available in literature that primarily focus on simpler geometries. The use of complex geometries necessitates the utilization of Cartesian grids, and as a result, there is a need to develop numerical frameworks capable of handling such Cartesian grids.

1.1 Motivation of the study

The scientific community generally prefers collocated meshes as the variables of interest are stored at the same location, typically cell-centers. However, these frameworks suffer from the pressure-velocity decoupling problem for incompressible flows. This issue is no longer a concern due to the Rhie-Chow interpolation [10] and its improvements. Despite this, the classical approach for incompressible fluid flows has utilized staggered meshes, which resolve the pressure-velocity decoupling problem by construction but lead to additional book-keeping as the quantities of interest are not all stored at the same location. There have been no significant efforts to compare their merits and drawbacks for the EHD flows with heat transfer. Both collocated and staggered grid approaches can work with unstructured meshes, but generating such meshes over complex geometries is a challenging task. Mesh generation can consume around 70% of the total cost of any simulation, and in design cycles, it can become a significant bottleneck, especially when dealing with complex geometries and multiple parametric studies requiring minor design changes. Moreover, when the geometries are in motion, flow solvers need to account for the mesh movement, and meshes must be regenerated if the deformation is significant. The strong correlation between grid quality and solution accuracy limits the usefulness of body-fitted finite-volume flow solvers, requiring additional effort to introduce improvements and fixes to handle large deformations and complex-shaped bodies.

In recent years, Cartesian-based approaches, such as immersed boundary (IB) methods, have gained popularity due to the simplicity of mesh generation algorithms.

IB methods are arguably the foremost among non-conformal techniques. Although there have been comparatively fewer applications of this technique (or its variants) for electro-hydrodynamics with heat transfer, a good review of immersed boundary approaches for incompressible flows can be found in [11]. Furthermore, studies in the EHD flows using conformal as well as non-conformal meshes have largely focused on the incompressible flow regime.

This thesis aims to develop direct forcing immersed boundary appraoch using finite-volume discretization for the EHD flows with heat transfer. The following sections will present a review of developments available in the literature, focusing on immersed boundary methods for electro-thermo hydrodynamic flows.

1.2 Physical background and related work

This section provides a comprehensive study of the different physical mechanisms inherent to the electro-thermo-convection problems. Specifically we focus on the configurations involving a hot cylinder immersed into a two-dimensional square enclosures as well as a hot sphere immersed into a three-dimensional cold cubic container. Despite the very simple geometry and boundary conditions, various complex physical phenomena occur in both configurations, which are explored and discussed in the course of this study

1.2.1 Pure thermal convection

Natural convection refers to the process of heat transfer in a fluid (such as a gas or liquid) due to the natural circulation of the fluid caused by temperature differences within it. This phenomenon is driven by the difference in density of the fluid at different temperatures, which creates buoyancy forces [12] that cause the fluid to move. This phenomenon occurs in a variety of problems, such as in the Rayleigh-Benard convection where a fluid layer heated from below and cooled from above, creating a temperature gradient [13, 14]. This causes the fluid to circulate, driven by the buoyancy forces resulting from the density differences in the fluid at different temperatures. A representative example is given in numerical study [15] in terms of distribution of

isotherms and streamlines as presented in Figure 1.1 for a natural convection around hot circular cylinder placed in a center of cold square cavity.

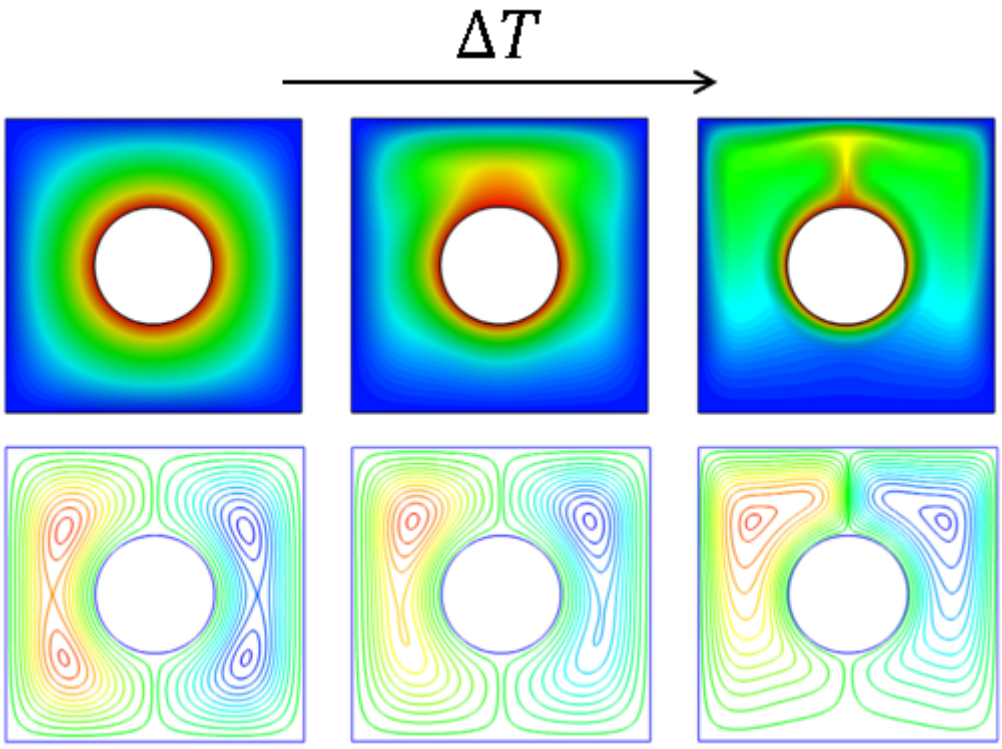

Figure 1.1: The effect of Rayleigh number on the temperature distribution (top) and streamlines (bottom) in 2D thermal flow [15].

At low temperature differences, the fluid motion is relatively small, and heat transfer is primarily driven by conduction. As the temperature difference increases, the strength of the buoyancy forces relative to the viscous forces increases, leading to more vigorous fluid motion and enhancing the heat transfer.

Figure 1.2 (b) shows a monotonic relationship between the Rayleigh number (Ra), and the induced fluid velocity. The increase in fluid velocity results in domination of the convection regime which in turn leads to increased heat flux from the cylinder surface. (see Fig.1.2)

1.2.2 Pure electro-convection

Electro-convection refers to fluid motion induced by an electric field to a dielectric liquid with a free charge carrier. This phenomenon arises from the interaction between the electric field and the fluid's charged particles (ions). The electric field exerts a force on

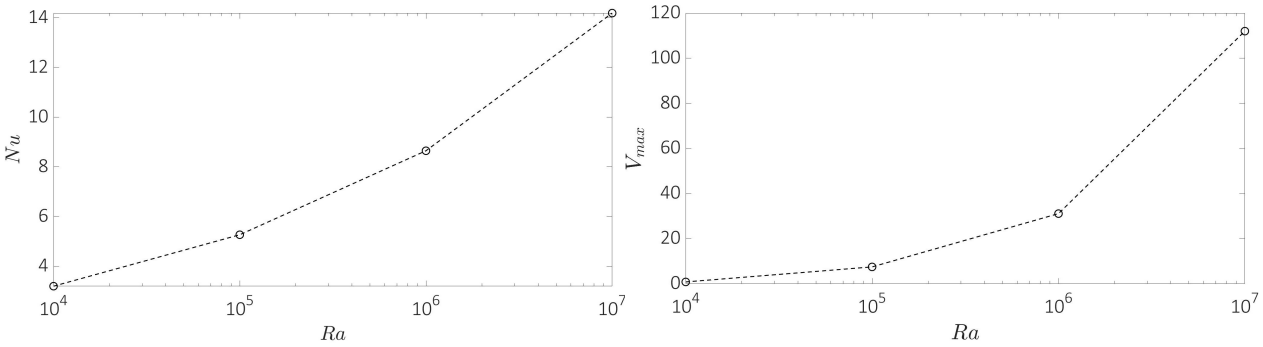

(a) (b)

Figure 1.2: A relationship between the Rayleigh number (a) and Nusselt number (B) and flow velocity [15]

.

the ions in the fluid, causing them to move and creating a net fluid flow. This mechanism can lead to various flow patterns, depending on the geometry of the system and the strength of the electric field [16].

Various sources, such as dissociation or charge injection at the liquid electrode interface, can generate the free charge carrier. The dominance of the injection mechanism is more significant than the other free charge sources; hence, in this work, we will refer exclusively to injection as a source of uni-polar charges [16].

The injection-induced electro-convection in the 2D cylinder-cube geometry shows a very different pattern compared to natural convection in the same geometry(see Figure 1.3). This behavior is because the buoyant thermal and Coulomb forces act in different directions. Also, the scalar fields of the temperature and the ionic concentration are transported via different mechanisms (conduction and electro-migration, respectively) in the inactive and weak flow motion state. The flow motion occurs only when the Coulomb force is strong enough to overcome the viscous forces. If the Coulomb force is not strong enough, the fluid remains in a rest state, and the migration transports free charges due to the electric field and molecular diffusion (the hydro-static state).

1.2.3 Electro-thermo-convection

Electro-thermo-convection (ETC) refers to fluid flows induced by the coupling of thermal, electric, and hydrodynamic effects in a fluid. This flow occurs when an electric

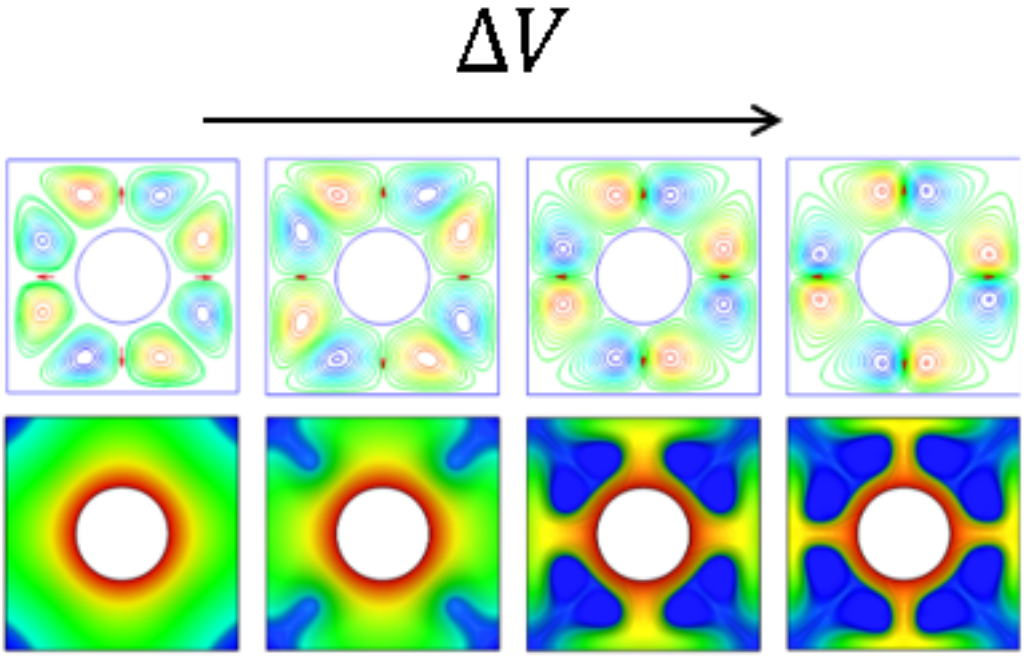

Figure 1.3: Illustration of the effect of increasing the potential difference on the streamlines and the charge distribution in two dimensions - pure electro-convection. [15]

field and temperature gradient are simultaneously applied to a fluid, generating fluid flow.

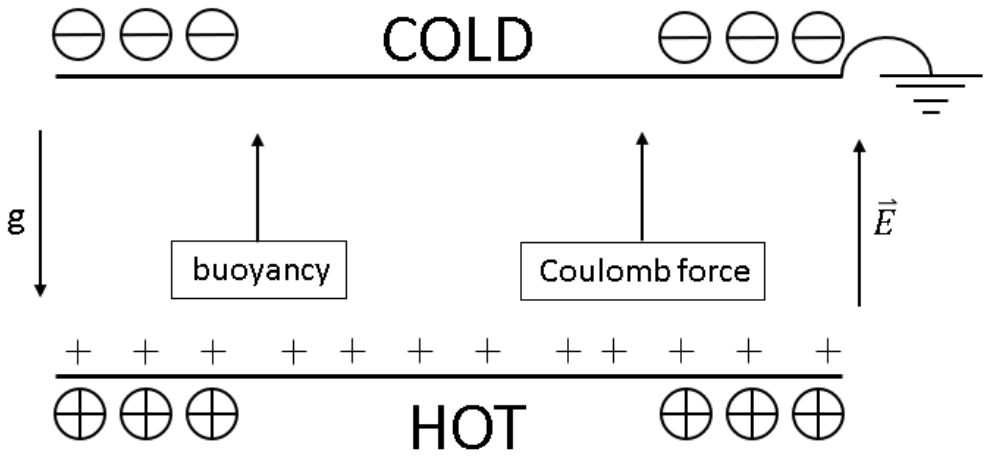

Figure 1.4: Schematic diagram of the buoyancy and electric fields in two-plate configuration

Figure 1.4 illustrates the combined effects of these forces on the fluid flow. The flow induced by the electric field can help or hinder the natural heat transfer mechanism. Therefore, in these applications, the direction of the electric field must be carefully

controlled to maximize heat convection. Experiments conducted at the beginning of the 1950s on the effect of the electric field in improving heat transfer in dielectric liquids [17–19] sparked significant research into the linear instabilities that arise due to the complex and strong nonlinear couplings between the different fields.

Most numerical and experimental research has focused on the basic configuration of two parallel plates [20–22] due to its similarity and comparison to the Rayleigh–Benard problem [13, 14]. However, due to the growing need for efficient cooling of various electronic components and high-power cables, and the potential use in cooling nuclear reactors, interest in the numerical analysis of more complex configurations has recently increased.

Figure 1.5 (a) shows the standard configurations used in these simulations. The spatial temperature distribution shown in Figure 1.5 (b) indicates that the effect of electric field induces a radial motion in the liquid which shows more uniform temperature distribution in a enclosure and as a result increasing the total heat transfer. Over the years, researchers have deeply studied the various stability criteria related to the liquid's properties, injection strength, and other physical parameters [23–26]. Most numerical and experimental research has focused on the basic configuration of two parallel plates [20–22] due to its similarity and comparison to the Rayleigh–Benard problem [13, 14]. Therefore, in recent years, most simulations of ETC have been performed in two-dimensional configurations with relatively simple geometry, such as a 2D cylinder inside a cube or a concentric ring, as they resemble a section cable in a liquid sheath [1].

The changes in the flow regime and temperature distribution illustrate the effect of the increase of electric field on the surrounding liquid, which induces a radial flow. It can be observed that when the electric field is weak, natural convection dominates the flow field and temperature distribution. However, for a stronger electric field the electro-convection becomes dominant, whereas the natural convection (resulted by the buoyancy force) becomes negligible. Remarkably that a relatively uniform temperature distribution in an enclosure is achieved along the radial movement causes an increase in the total heat transfer.

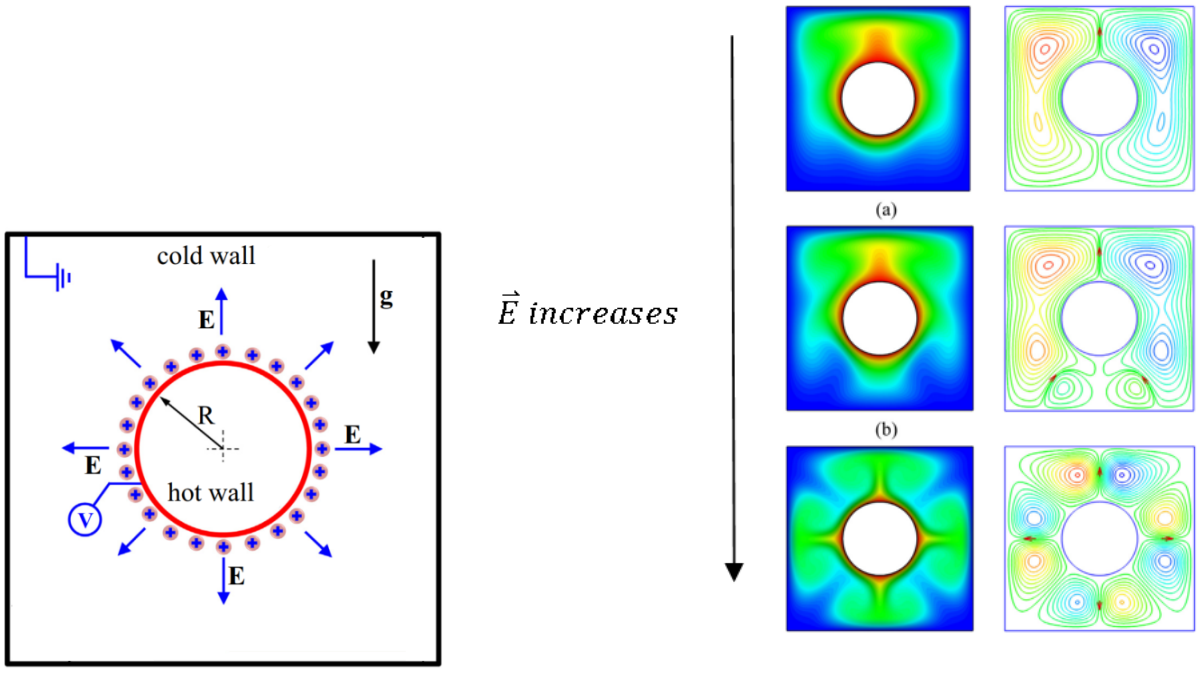

Figure 1.5: (a) diagram of 2D annular cavity (b) the effect of electric field on the temperature distribution

1.3 Computational approaches

To simulate electrically-driven Flow (EDF) phenomenon, it is essential to establish a mathematical model that links the charge density distribution, the electric potential, and the flow fields. The model should address the mutual influence of flow and electric force. There are several models used to study the EDF, including the Poisson-Nernst-Planck (P-NP) [27, 28], Poisson-Boltzmann (PB) [29], and Debye-Huckel (DH) [30] models. Each model has its strengths and limitations. The P-NP model is the most comprehensive and suitable for time-dependent problems. It includes the Poisson equation for the potential distribution as a function of the spatial free charge distribution and a conservation equation (Nernst-Planck) for the charge density distribution. The total flux in the conservation equation includes the convection and diffusion terms, as well as the electro-migration term, which reflects the flux effect by the electric force. The PB model is useful for simulating systems with a low ion concentration based on the Poisson equation, it includes the Boltzmann distribution function to describe the ion

concentration. Moreover, the DH model is appropriate for highly diluted systems and developed to explain the behavior of weak electrolytes, and is based on the assumption of a constant dielectric constant and a uniform electric field. Following the benefits and disadvantages listed above, we use the P-NP model in this work.

1.3.1 Immersed boundary method for EHTD

Numerical simulation of the flows developing around solid bodies of irregular geometry can be challenging as it requires building body fitted grids. The Immersed Boundary (IB) method initially developed by Peskin [31, 32] can remedy the above difficulty. This method provides an alternative approach for adapting the computational grid to the geometry of a body by representing the body with by a series discrete Lagrangian points. These points do not necessarily coincide with the original Eulerian grid. A volumetric force term is added to the momentum equation to enforce the no-slip kinematic constraint in the Lagrangian points. These forces replace the body's effect on the flow around it, and for each Lagrangian point, the kinematic constraint is added as an additional equation, requiring the same values of the body surface velocity and the the flow velocity interpolated to the Lagrangian point of the body surface. This set of volumetric forces plays the role of the Lagrange multipliers. A closed form of the overall equation system incorporating the flow variables and the volumetric forces along with the kinematic constraints of no-slip is eventually obtained [11].

Since the Lagrangian points do not necessarily align with the Eulerian grid, it is necessary to introduce interpolation operator interpolating the Eulerian velocities to the corresponding Lagrangian points from the Eulerian grid to the Lagrangian points. A regularization operator should be also defined as an adjoint to the interpolation operator to convey an information from the Lagrangian points to the Eulerian grid. Both operators are implemented by using the discrete delta function allowing for their efficient embedding in the discrete set of equations [33].

The IB method can be used to enforce appropriate boundary conditions for additional physical equations coupled to the flow equations. For example, a constant wall temperature in the energy equation can be obtained by adding a heat flux term to the energy equation and a constraint equation to the desired boundary condition

[12, 34–37]. Also, additional boundary conditions can be implemented using the IB method, such as Neumann and Robin type boundary conditions, but their implementation is not immediate and requires the adoption of another auxiliary algorithms such as ghost cell, phase field method, etc. [38, 39]

Historically, the IB method was implemented explicitly. The volumetric force added to the momentum equation was first calculated by basing on a predictor equation solved without considering the IB constraints. However an implicit implementation of the IB method can typically provide more accurate imposing of the kinematic constraints. Implicit implementation of the IB method relaxes the need of progressing by a very small time steps and reduces the flow leakage through the boundaries of the immersed body. [40]

In recent years, the IB method has been extensively used for studying natural convection in enclosures with embedded discrete thermally active sources of various geometries [12, 41, 42]. An algorithm which allows for efficient simulation of thermally driven flows the developing around immersed bodies in 3D has been recently established by [12]. In this approach, the energy equation is coupled with the momentum equations by using a Boussinesq approximation. The SIMPLE algorithm is utilized for the pressure-velocity coupling [43], and the kinematic constraints introduced by the IB method appear as Lagrange multipliers. The kinematic constraints for the temperature of the surface of the immersed body are implemented by the same IB formalism.

It is apparent that there is a lack of numerical investigations using the immersed boundary approach for standard thermo-electro-hydrodynamic problems in the incompressible regime. The above gap can be apparently attributed to the difficulties which can rise when extending the IB functionality to the P-NP system of equations, governing the thermo-electro-hydrodynamic regime.

1.4 Objectives of the study

As stated in this chapter, the primary aim of this thesis is to develop an immersed boundary/finite volume framework capable of simulating electro-hydrodynamics flows with heat transfer. Based on the literature review of numerical methods in electro-

hydrodynamics flows with heat transfer, particularly those utilizing the IB approach, we have specified the following specific sub-objectives for this research work.

- **Development of a direct forcing immersed boundary method based on staggered finite volume framework**: We developed a three-dimensional boundary/finite volume (IB-FV) solver designed for the simulation of electro-hydrodynamic flows with heat transfer based on the direct forcing immersed boundary approach in a staggered framework. The direct forcing IB method employs a technique, initially introduced in [12], which allows for the construction and solution of modified governing equations throughout the domain. The governing equations for mass, momentum and energy are solved in a similar manner to the direct forcing IB method as discussed in [12]. We also solve the electric potential and the charge density equations utilizing the direct forcing approach.

The numerical investigations will be carried out for uni-polar dielectric liquid placed in three-dimensional enclosure. The parametric study is performed with the aim of enhancing heat transfer from the surface of immersed body.

1.5 Outline of thesis

The thesis is structured as follows: Chapter 2 introduces the governing equations of the EHD flow coupled with heat transfer and presents a finite volume discretization implemented on a staggered grid. Chapter 3 describes the direct forcing immersed boundary IB-FV framework for thermo-electro-hydrodynamic flows. Chapter 4 presents results of the performed numerical simulations and focuses on the revealed physical insights. Finally, Chapter 5 provides an overview of the main contributions of the thesis and suggests possible directions for future research.

CHAPTER 2

GOVERNING EQUATIONS AND SOLUTION METHODOLOGY

This chapter is devoted to a concise description of the mathematical formulations governing incompressible flows. We give the non-dimensional conservative equations governing the considered electro-thermally driven flows. The governing equations are disretized by the finite volume method. The standard staggered grid approach is utilized to distinguish between the scalar fields and components of the vector fields. The proposed methodology and its implementations in our in-house flow solver are discussed in detail.

2.1 Governing equations

The focus of our study is on the electro-thermo-hydrodynamics which combines the the phenomena observed in fluid mechanics, heat transfer, and electro-kinetics. The flow is governed by the system of continuity, momentum, energy, electro-static and the charge density conservation equations:

$$\tilde{\nabla} \cdot \tilde{\mathbf{u}} = 0 \tag{2.1}$$

$$\frac{\partial(\rho_o \tilde{\mathbf{u}})}{\partial t} + \tilde{\nabla} \cdot (\rho_o \tilde{\mathbf{u}} \tilde{\mathbf{u}}) = -\tilde{\nabla} \tilde{P} + + \rho_o \nu \tilde{\nabla}^2 \tilde{\mathbf{u}} + \tilde{q} \tilde{\nabla} \tilde{\phi} - \tilde{\rho} \mathbf{g} \tag{2.2}$$

$$\frac{\partial \tilde{\theta}}{\partial \tilde{t}} + \tilde{\nabla} \cdot (\tilde{\mathbf{u}}\tilde{\theta}) = \frac{\kappa}{\rho_o C_p} \tilde{\nabla}^2 \tilde{\theta}, \tag{2.3}$$

$$\tilde{\nabla}^2 \tilde{\phi} = -\frac{\tilde{q}}{\varepsilon}, \tag{2.4}$$

$$\frac{\partial \tilde{q}}{\partial \tilde{t}} + \tilde{\nabla} \cdot (\tilde{q}\tilde{\mathbf{u}} - K\tilde{q}\tilde{\nabla}\tilde{\phi} - D\tilde{\nabla}\tilde{q}) = 0, \tag{2.5}$$

where $\tilde{\mathbf{u}}$ denotes the velocity vector$[\tilde{u}, \tilde{v}, \tilde{w}]$, $\tilde{P}$ is the hydrodynamic pressure, $\tilde{\theta}$ refers to the temperature field, $\tilde{\phi}$ is the electric potential, and $\tilde{q}$ is the charge density field. The effect of gravity and electric field is accounted as a source term in the momentum equation. K denotes the ionic mobility, $\tilde{\rho}$ is the fluid density, ν represents the kinematics viscosity, κ is the thermal conductivity, and ε is the electrical permittivity. $\mathbf{g}$ is the gravity vector, D refers to the molecular diffusion coefficient, and $\tilde{t}$ is the time. ρ_0, represents the density field corresponding to the reference temperature, θ_0. β is the coefficient of thermal expansion. The generic subscript symbol $\sim$ corresponds to a dimensional form of the equations.

We next non-dimensionalise the above governing equations using a suitable reference scales as given below,

$$\begin{gathered}\mathbf{x} = \frac{\tilde{\mathbf{x}}}{H}, \quad t = \tilde{t}\frac{\nu}{H^2}, \quad \mathbf{u} = \tilde{\mathbf{u}}\frac{H}{\nu}, \quad p = \tilde{p}\frac{H^2}{\rho_0 \nu^2}, \phi = \frac{\tilde{\phi}}{\Delta\phi}, \quad q = \frac{\tilde{q}}{q_0}, \\ \rho = \frac{\tilde{\rho}}{\rho_0}, \quad \theta = \frac{\tilde{\theta} - \theta_0}{\Delta\theta}\end{gathered} \tag{2.6}$$

where $\mathbf{x}$ is geometric coordinates in X, Y and Z direction, H and q_0 refer to characteristic length and charge density scales, respectively. $\Delta\phi$ denotes the potential difference $\phi_0 - \phi_1$ and $\Delta\theta$ is the temperature difference $\theta_h - \theta_c$. The cold and hot temperatures are defined as θ_c and θ_h, respectively. We choose the velocity scale based on the kinematic viscosity which arguably the physically correct choice of a reference velocity for electro-thermally driven flows. Other choices of velocity scale are also possible, although they would result in a different form of the non-dimensional governing equations. The obtained non-dimensional equations govern the behavior of the fluid in a way that is independent of the specific values of the reference quantities, making it easier to compare and analyze results for different flow problems.

$$\nabla \cdot \mathbf{u} = 0 \tag{2.7}$$

$$\frac{\partial \mathbf{u}}{\partial t} + \nabla \cdot (\mathbf{u}\mathbf{u}) = -\nabla P + \nabla^2 \mathbf{u} - \frac{T^2}{M^2} C q \nabla \phi - \frac{Ra}{Pr} \theta \vec{e_z}, \tag{2.8}$$

$$\frac{\partial \theta}{\partial t} + \nabla \cdot (\mathbf{u}\theta) = \frac{1}{Pr} \nabla^2 \theta, \tag{2.9}$$

$$\nabla^2 \phi = -C \cdot q, \tag{2.10}$$

$$\frac{\partial q}{\partial t} + \nabla \cdot (\mathbf{u} q) = \hat{D} \nabla^2 q + \nabla \cdot (q \frac{T}{M^2} \nabla \phi). \tag{2.11}$$

The non-dimensional groups appearing in the equations are the Prandtl number Pr, Rayleigh number Ra and the electric Rayleigh number T defined as:

$$Ra = \frac{\vec{g} \beta \Delta \theta H^3}{\kappa \nu}, \quad Pr = \frac{\nu}{\alpha_0}, \quad T = \frac{\varepsilon \phi_0}{\rho \nu K} \tag{2.12}$$

The other non-dimensional coefficient appearing in equations are the injection strength number C, the mobility number M and the molecular diffusion coefficient $\hat{D}$ defined as:

$$C = \frac{q_0 H^2}{\varepsilon \phi_0}, \quad M = \frac{1}{K} \sqrt{\frac{\varepsilon}{\rho}}, \quad \hat{D} = \frac{D}{\nu} \tag{2.13}$$

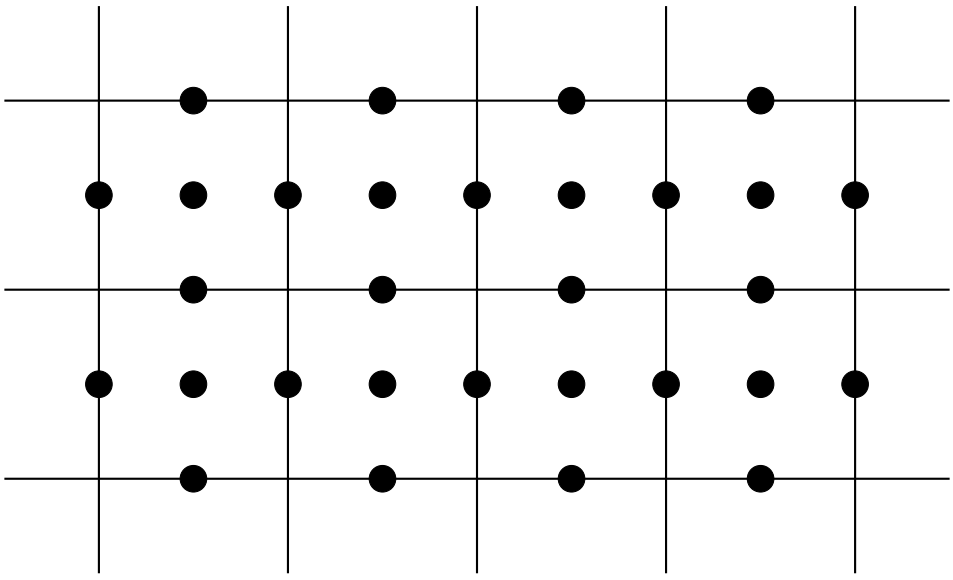

Figure 2.1: Staggered grid arrangement

2.2 Staggered grid discretization

The success of any numerical algorithm in adressing the problem depends on two key factors: the choice of variable arrangement on the computational grid, and the discretization approach used to approximate the governing equations. Two commonly used variable arrangements are the collocated and the staggered arrangements. These arrangements differ in the way the different fields are discretized on the grid relatively to each other. The choice of the arrangement of the fields can have a significant impact on the accuracy and stability of the numerical solution, and different arrangements may be more suitable for different types of problems or numerical methods. Therefore, careful consideration of the variable arrangement and discretization approach is crucial for the development of an effective numerical algorithm solving computational fluid dynamics problems. In the collocated framework, all variables are lumped at the same location, typically the cell-center. On the other hand, in the staggered framework, the velocity is stored at the faces of the cells while all the scalar fields (including pressure temperature and electric potential fields) are stored at the centroid of the cell, as shown in Figure 2.1. While other variable staggering techniques exist, the conventional numerical frameworks have mostly favored the collocated framework, particularly on unstructured meshes. However, the collocated framework suffers from a phenomenon known as pressure-velocity decoupling, also referred to as the "checkerboard" pattern, in incompressible flows. This issue can be remedied by using techniques such as Rhie-Chow interpolation or related methods. In contrast, staggered frameworks do not suffer from the pressure-velocity decoupling, but they require additional book-keeping and are not as straightforward to implement on arbitrary polygonal meshes. Ultimately, the choice between collocated and staggered frameworks depends on the specific requirements of the problem and the numerical method being used. Both frameworks have their advantages and disadvantages, and the choice of a spesific framework should be based on a careful analysis of the trade-offs involved. In the current study we utilize the staggered grid for discretization of the governing equations. The numerical algorithm used to discretize the governing equations is based on a finite volume approach.

2.3 Momentum equation

The convective flux in the momentum equation is discretized using second-order upwind schemes, while the diffusive flux is discretized using central difference schemes. The momentum equation's semi-discrete form is expressed as follows:

$$\frac{d\mathbf{u}}{dt}\,\Omega + \underbrace{\Big[\sum_{e\in\Omega}(\mathbf{u}_e\mathbf{u}_e\cdot\mathbf{n}_e)\Delta s_e\Big]}_{\mathbb{CONV}} = -\frac{\delta p}{\delta n}\Omega + \underbrace{\Big[\sum_{e\in\Omega}(\nabla\mathbf{u}_e\cdot\mathbf{n}_e)\Delta s_e\Big]}_{\mathbb{DIFF}} - \frac{T^2}{M^2}Cq\nabla\frac{\delta\phi}{\delta n}\Omega - \frac{Ra}{Pr}\theta\Omega\vec{e_z} \tag{2.14}$$

where Δs_e represents the surface area of the edge e, and Ω is the control volumes for momentum equation. The discrete convective and diffusive fluxes are denoted as $\mathbb{CONV}$ and $\mathbb{DIFF}$, respectively, and their discretization is discussed below.

2.4 Convective flux discretization

The convective flux appearing in the momentum equation Eqn. 2.14 is written in a discrete form as,

$$\sum_{e\in\Omega}(\mathbf{u}_e\mathbf{u}_e\cdot\mathbf{n}_e)\Delta s_e \;=\; -\sum_{e\in\Omega}\begin{pmatrix} u_eU_e\Delta\mathrm{S}_e \\ v_eU_e\Delta\mathrm{S}_e \\ w_eU_e\Delta\mathrm{S}_e \end{pmatrix} \tag{2.15}$$

Where u_e, v_e and w_e refer to the Cartesian components of velocity at the face e, and U_e is the normal velocity at the face e. The $\mathbf{u}_e$, $\mathbf{v}_e$, and $\mathbf{w}_e$ are computed at the interfaces of the control volume using the Second Order Upwind (SOU) scheme.

2.5 Diffusive flux discretization

The diffusive flux contribution to the flux term in Eqn.2.14 is given by,

$$\sum_{e\in\Omega}(\nabla\mathbf{u}_e\cdot\mathbf{n}_e)\Delta s_e = -\sum_{e\in\Omega}\begin{pmatrix}\left.\frac{\delta u}{\delta n}\right|_e \Delta \mathrm{S}_e \\ \left.\frac{\delta v}{\delta n}\right|_e \Delta \mathrm{S}_e \\ \left.\frac{\delta w}{\delta n}\right|_e \Delta \mathrm{S}_e\end{pmatrix}$$

2.6 Temporal discretization of momentum equation

To attain second-order temporal accuracy, we utilize a three-point backward differencing (BDF2) scheme for temporal discretization. Our flow solver utilizes the SIMPLE algorithm [43] for the pressure-velocity coupling. The predictor step's discrete form is as follows:

$$\begin{aligned}\frac{3\mathbf{u}_c^\star - 4\mathbf{u}_c^n + \mathbf{u}_c^{n-1}}{2\Delta t}\Omega = &-\mathbb{CONV}(\mathbf{u}_e^n,\mathbf{u}^n) + \mathbb{DIFF}(\mathbf{u}_e^n,\mathbf{u}^n) - \frac{\delta p}{\delta n}\Omega \\ &- \frac{T^2}{M^2}Cq\nabla\frac{\delta\phi}{\delta n}\Omega - \frac{Ra}{Pr}\theta\Omega\vec{e_z}\end{aligned} \tag{2.16}$$

where $\mathbf{u}_e^\star$ refers to the momentum at the intermediate time level between $n+1$ and n. The value of momentum at predictor step would not satisfy the continuity constraint in general. We note that the term corresponding to the convective flux in the momentum equation was taken from the previous time step..

2.7 Pressure correction equation

The hydrodynamic pressure appearing in the momentum equation does not have a natural evolution equation. We obtain an equation for pressure correction by subtracting the momentum equation at $'*'$ and $(n+1)th$ time level which gets:

$$\frac{3}{2}\frac{(\mathbf{u}_c^{n+1} - \mathbf{u}_c^\star)}{\Delta t} = -\frac{\delta\Phi}{\delta n} \tag{2.17}$$

where $\Phi = P^{n+1} - P^n$ refers to the pressure correction. It should be noted that Eqn. 2.17 is only an approximation since it neglects the differences between the convective and diffusive flux contributions, which can introduce second-order errors. Summing up Eqn. 2.17 over all the faces of any given cell yields an expression for the total pressure

correction within the cell:

$$\frac{3}{2}\sum_{e\in\Omega}\mathbf{u}_e^{n+1}\Delta s_e - \frac{3}{2}\sum_{e\in\Omega}\mathbf{u}_e^{\star}\Delta s_e = -\Delta t\sum_{e\in\Omega}\frac{\delta\Phi}{\delta n}\Big|_e\Delta s_e \tag{2.18}$$

The Eqn. 2.18 is derived by summing Eqn. 2.17 over all faces of a cell can be interpreted as a discrete Poisson equation for the correction to hydrodynamic pressure, denoted by Φ. However, it is important to note that the term $\sum_{e\in\Omega}\mathbf{u}_e^{n+1}\Delta s_e$ represents the discrete divergence constraint at the $(n+1)th$ time level and is typically neglected for incompressible flows. Therefore, for incompressible flows, this term can be disregarded, resulting in a simplified form of the discrete Poisson equation for the hydrodynamic pressure correction:

$$\sum_{e\in\Omega}\mathbf{u}_e^{\star}\Delta s_e = \frac{2}{3}\Delta t\sum_{e\in\Omega}\frac{\delta\Phi}{\delta n}\Big|_e\Delta s_e \tag{2.19}$$

The discrete normal gradient of pressure correction at the faces e is represented by $\frac{\delta\Phi}{\delta n}\Big|_e$, and the left-hand side of the equation is obtained from the solution of the momentum equation. In contrast to the momentum equation, the control volume for the pressure correction equation is the individual cell, since the pressure and its correction are stored at the cell centroids. The normal derivative for pressure correction is discretized by using central difference scheme.

2.8 Energy equation

The energy equation is solved with convective and diffusive flux discretization similar to that used for the momentum equation. This equation solves for temperature and is integrated over a single cell, hence it has a control volume different from that used for the normal momentum equation. The energy is a scalar quantity, much like the pressure correction equation, and is stored at the cell centroid. Integrating the thermal energy equation over the control volume reads,

$$\oint_{\Omega_c}\frac{\partial\theta}{\partial t}\,d\Omega + \oint_{\Omega_c}\nabla\cdot(\mathbf{u}\theta)\,d\Omega = \oint_{\Omega_c}\frac{1}{Pr}\nabla^2\theta\,d\Omega \tag{2.20}$$

The discrete form of Eqn. 2.20 can be obtained by applying the Gauss divergence theorem to the remaining terms. This gives an expression that can be written as follows

$$\frac{3\theta_c^{n+1} - 4\theta_c^n + \theta_c^{n-1}}{2\Delta t}\Omega_c + \sum_{e\in\Omega} \mathbf{u}_e\theta_e\Delta s_e = \frac{1}{Pr}\sum_{e\in\Omega}\frac{\delta\theta}{\delta n}\Big|_e \Delta s_e \tag{2.21}$$

In the discrete form of Eqn.2.21 $e \in \Omega$ denotes the edges of the control volume and Ω_c refers to the area of the control volume. The velocity $(\mathbf{u}_e)$ at edge e is obtained from the solution of the momentum equation and represents the convecting velocity for the energy field. The convective flux $(\mathbf{u}_e\theta_e)$ at edge e is calculated using a second-order upwind scheme. The fluxes in the energy equation are evaluated at the cell edges e in a similar manner as in the momentum equation. The normal derivative of temperature $\frac{\delta\theta}{\delta n}\Big|_e$ at the cell edges is obtained analogously to that for the pressure correction as described in Section 2.7. To solve the energy equation (Eqn. 2.21), a known velocity field at a particular time-step is assumed, which is obtained from the solution of the momentum equation in the previous time-step. This results in a linearized system of equations due to the implicit treatment of non-linear terms. The temperature at the cell centroids can be obtained by solving the resulting system of equations with a sub-iteration loop, similar to that used for the pressure correction equation.

2.9 Charge transport equation

The charge transport equation is solved using a collocated framework that involves discretizing convective and diffusive fluxes, similar to what is done for the energy equation. The equation is used to solve for the charge and is integrated over a single cell, which has the same control volume used for the energy equation (since the charge transport equation is a scalar quantity, it is stored at the cell centroid). The integration of the charge transport equation over the control volume yields,

$$\oint_{\Omega_c} \frac{\partial q}{\partial t}\, d\Omega + \oint_{\Omega_c} \nabla\cdot(\mathbf{u}q)\, d\Omega = \oint_{\Omega_c} \hat{D}\nabla^2 q\, d\Omega + \oint_{\Omega_c} \nabla\cdot(q\frac{T}{M^2}\nabla\phi)\, d\Omega \tag{2.22}$$

To derive the discrete form of Eqn. 2.22, the Gauss divergence theorem is applied to the remaining terms, resulting a finite volume formulation of the charge transport

equation:

$$\frac{3q_c^{n+1} - 4q_c^n + q_c^{n-1}}{2\Delta t}\Omega_c + \sum_{e\in\Omega} \mathbf{u}_e q_e \Delta s_e = \hat{D} \sum_{e\in\Omega} \frac{\delta q}{\delta n}\Big|_e \Delta s_e + \frac{T}{M^2} \sum_{e\in\Omega} \mathbf{u}_e q_e \frac{\delta \phi}{\delta n}\Big|_e \Delta s_e \quad (2.23)$$

The convecting velocity for the charge transport field, represented by the velocity $(\mathbf{u}_e)$ at edge e, is from the solution of the momentum equation. The convective flux $(\mathbf{u}_e q_e)$ at edge e is approximated using a second-order upwind scheme, and the other fluxes in the charge equation are evaluated at the cell edges e in a manner similar to that in the energy equation. The normal derivative of charge $\frac{\delta q}{\delta n}\Big|_e$ and electric potential $\frac{\delta \phi}{\delta n}\Big|_e$ at the cell edges are obtained using an analogous method to that described in Section 2.7 for the pressure correction. To solve the discrete charge transport equation (Eqn. 2.23), the flow velocity is taken from the previous time step.

2.10 Solution methodology

In the present work, an incremental fractional step method is used to solve the equations in a segregated manner. Initially, the electric potential equation is solved at the cell center assuming the charge density from the previous time level. Next, the charge transport equation is solved at the cell centers for charge, assuming the velocity field from the previous time level as the initial conditions for the first time step. Next, the energy equation is solved for temperature at the cell centers, assuming the velocity field from the previous time level as was performed for the solution of the charge equation. Next, the momentum equation is solved using the pressure field at the $n-th$ time level, which still does not satisfy the divergence free constraint on the velocity field. In the next step the Poisson equation is solved for the pressure correction field. The obtained pressure correction field is then used to update the pressure and to project the predicted velocity field on the divergence free subspace as follows:

$$P^{n+1} = P^n + \Phi \quad (2.24)$$

$$\mathbf{u}^{n+1} = \mathbf{u}^\star - \frac{2}{3}\Delta t \frac{\delta \Phi}{\delta n}\Big|_e \quad (2.25)$$

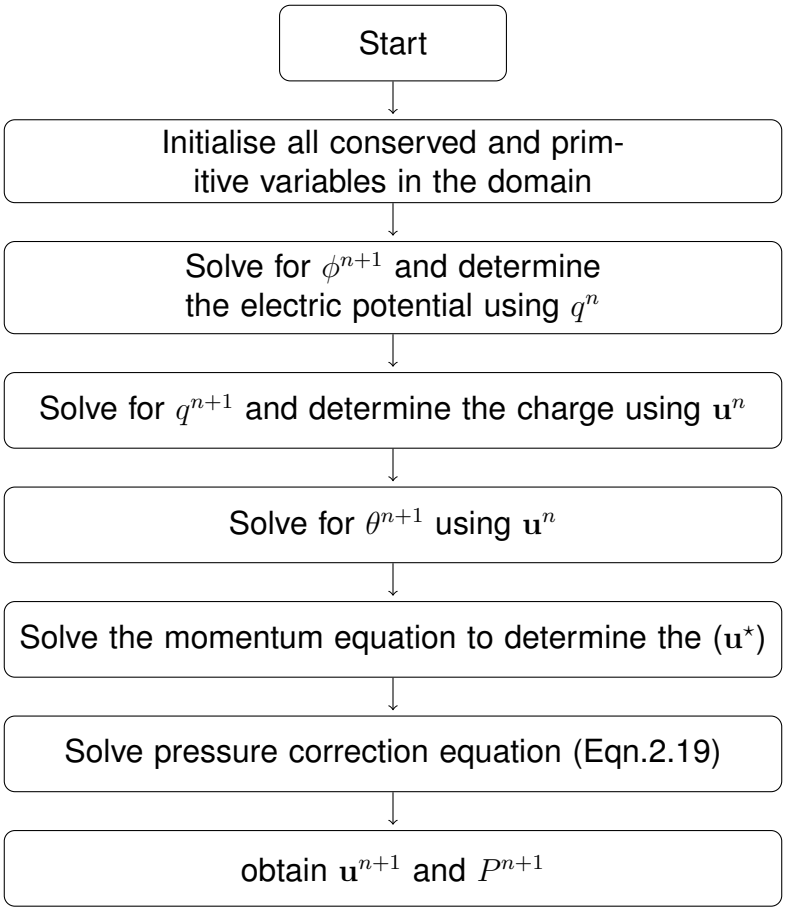

Figure 2.2: Flowchart for solution methodology of staggered framework.

The solution flowchart is illustrated in Figure 2.2, which serves as a quick reference for the finite volume flow solver that forms the basis of the research. The details of the immersed boundary methodology and its application for the simulation of the Boussinesq flows are discussed in Chapter 3.

CHAPTER 3

DIRECT FORCING IMMERSED BOUNDARY FORMULATION

In this Chapter, we will give a brief overview of the direct forcing immersed boundary method, which is used to study electro-thermobuoyant flows. This method involves the direct imposition of forces onto the fluid in order to account for the presence of solid objects or other obstacles within the flow field. The method formulates modified governing equations by adding force terms to account for the presence of solid objects. The force terms are derived based on the geometry and kinematics of the solid object, and are then applied to the fluid in a way that accounts for the interaction between the fluid and the object. The discretized equations are then solved using either the staggered or non-staggered finite volume framework, which was previously described in Chapter 2. The accuracy and versatility of the immersed boundary framework are demonstrated through the numerical simulation of several canonical fluid flow problems, including those involving electro-thermobuoyant flows. This technique provides an efficient and reliable methodology for simulating complex electro-thermo-hydrodynamic flow phenomena.

3.1 Direct forcing immersed boundary method

This Chapter focuses on describing the direct forcing immersed boundary (IB) method used in conjunction with a staggered finite volume framework, as explained in Chapter 2. This method involves a solving two separate equations for the fluid velocity and the force exerted by the solid boundary. The force term is then explicitly added to the fluid equation to account for the effect of the boundary on the fluid flow. In this thesis, a unique immersed boundary finite volume framework has been developed by leveraging this philosophy, which enables the solution of electro-thermo hydrodynamic flows.

3.2 Modified governing equation

The direct forcing immersed boundary approach is based on the principle of solving unified modified governing equations throughout the entire computational domain. The governing equations augmented with the IB functionality can be written as:

$$\nabla \cdot \mathbf{u} = 0 \tag{3.1}$$

$$\frac{\partial \mathbf{u}}{\partial t} + \nabla \cdot (\mathbf{u}\mathbf{u}) = -\nabla P + \nabla^2 \mathbf{u} - \frac{T^2}{M^2} C q \nabla \phi - \frac{Ra}{Pr} \theta \vec{e_z} + \vec{f_{\mathbf{u}}}, \tag{3.2}$$

$$\frac{\partial \theta}{\partial t} + \nabla \cdot (\mathbf{u}\theta) = \frac{1}{Pr} \nabla^2 \theta + f_\theta, \tag{3.3}$$

$$\nabla^2 \phi = -C \cdot q + f_\phi, \tag{3.4}$$

$$\frac{\partial q}{\partial t} + \hat{D} \nabla^2 q = \nabla \cdot (q \frac{T}{M^2} \nabla \phi - q\mathbf{u}) + f_q, \tag{3.5}$$

where the volumetric source/force f_ψ reflects the impact of the immersed body on the surrounding field ψ and can be defined as:

$$f_\psi(x_i) = \int_S F_\Psi^K(X^K) \cdot \delta(x_i - X^K) dV_S^K \tag{3.6a}$$

$$\Psi(X^K) = \int_\Omega \psi(x_i) \cdot \delta(X^K - x_i) dV_{\Omega_i} \tag{3.6b}$$

where δ is the discrete Dirac function. The function introduced by Roma et al.

in [44], utilized in the current study is given by:

$$\delta(r) = \begin{cases} \frac{1}{6\Delta r}\left[5 - 3\frac{|r|}{\Delta r}] - \sqrt{-3(1-\frac{|r|}{\Delta r})^2 + 1}\right] & \frac{1}{2}\Delta r \leq |r| \leq \frac{3}{2}\Delta r \\ \frac{1}{3\Delta r}\left[1 + \sqrt{-3(\frac{|r|}{\Delta r})^2 + 1}\right] & |r| \leq 0.5\Delta r \\ 0 & \text{otherwise} \end{cases} \tag{3.7}$$

Here, Δr is the cell width in the r direction, which means that the above delta function supports three grid cells in each spatial direction, when employed in interpolating Eulerian fields $\psi(x_i)$ and regularizing Lagrangian forces F_Ψ^K. The chosen delta function has been specifically designed for performing calculations on staggered grids and has gained popularity over recent years [45], [46], [47] due to its compact kernel (only 3 cells in each direction of the computational domain). Interpolation of the discrete Eulerian fields $\psi(x_i)$ and regularization of the discrete Lagrangian source F_Ψ^K for the 3D configuration are performed by employing the following formulas:

$$f_\psi(x_i) = \Delta x \Delta y \Delta z \sum_i F_\Psi^K(X^K)\delta(|x_i - \varepsilon_K|)\delta(|y_i - \eta_K|)\delta(|z_i - \zeta_K|) \tag{3.8a}$$

$$\Psi(X^K) = \Delta x \Delta y \Delta z \sum_K \psi(x_i)\delta(|x_i - \varepsilon_K|)\delta(|y_i - \eta_K|)\delta(|z_i - \zeta_K|), \tag{3.8b}$$

where ε_K, η_K and ζ_K correspond to X, Y and Z components of the Lagrangian point K respectively.

The spatial discretization used is implemented on a staggered Eulerian grid, where the different velocity components are offset from one another and from the other scalar fields located in the center of the computational cell. An arbitrary object with an irregular shape, S, is immersed within a computational domain, Ω, and its surface is defined by a set of Lagrangian points, X^K. This surface, represented by ∂S, does not necessarily conform to the underlying spatial grid. At each Lagrangian point, appropriate volumetric forces, $\vec{f}_{\mathbf{u}}$, heat sources, f_θ, charge injection, f_q, and electric potential sources, f_ϕ, are applied to enforce all physical (dynamic) boundary conditions along ∂S. Closed form of the overall system of equations is obtained by augmenting it with equations governing the kinemtic constraints of the problem. The values of these sources are

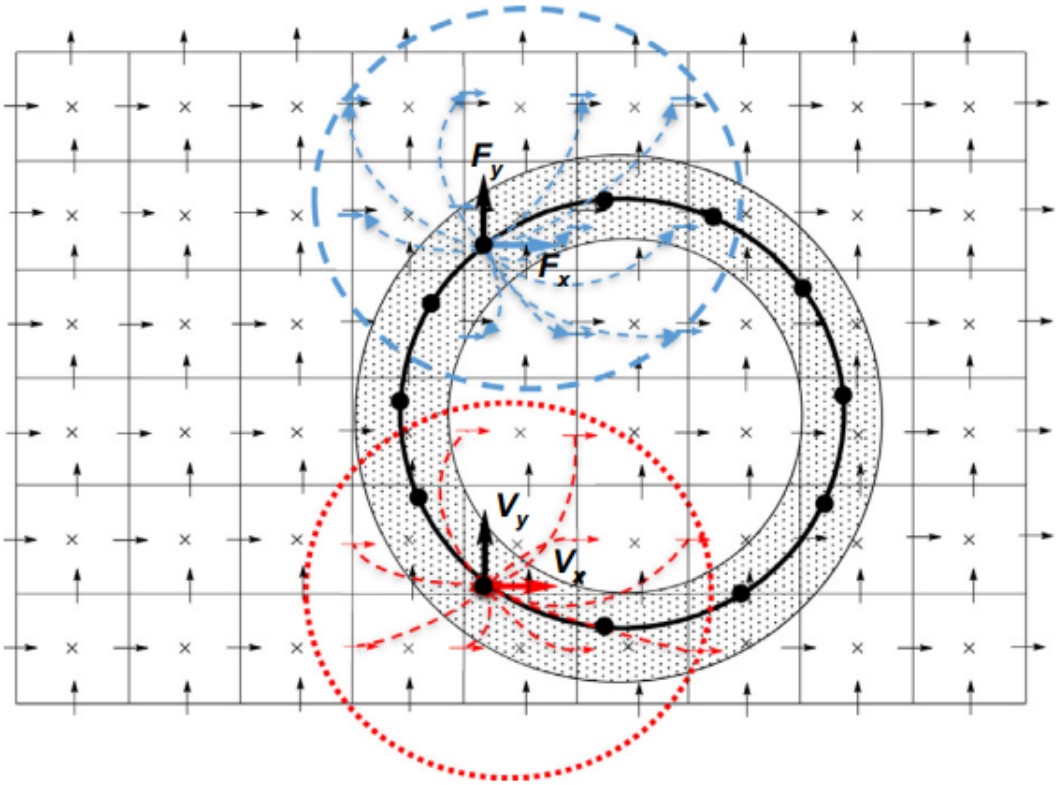

Figure 3.1: A schematic representation of the major principles of the IBM. The immersed body of elliptical shape is described by set of Lagrangian points indicated by the full black dots. A dashed shell of thickness equal to one grid step, attached to the immersed body,corresponds to the set of discrete volumes surrounding each Lagrangian point. The dashed and dotted circles show the range of action of the regularized Dirac delta functions smearing the Lagrangian forces over the Eulerian grid and interpolating the Eulerian velocities at the Lagrangian points, respectively. Adapted from [12]

then directly accounted for in the overall balance, enabling the direct calculation of the Nusselt number, which is the average of the heat sources, f_θ.

As the location of the boundary represented by the Lagrangian points does not necessarily coincide with the underlying spatial discretization, regularization and interpolation operators must be defined to convey information in both directions of the body grid. The regularization operator smears Lagrangian volumetric sources, F_Ψ^K (where Ψ corresponds to a specific Lagrangian field) on the nearby Eulerian computational domain. The interpolation operator, on the other hand, acts in the opposite direction by interpolating the Eulerian fields ψ to the Lagrangian points X^K. Figure 3.1 shows a typical setup of the Eulerian grid and the Lagrangian points with an illustration of the

regularization and interpolation operators of the Lagrangian forces.

3.3 Solution methodology of IBM

The momentum, energy, electric potential, and charge equations in the direct forcing method are influenced by the forcing function, whereas the Poisson equation for pressure correction is not affected by it. The Poisson equation is solved throughout the domain, and the Neumann boundary condition for pressure correction is implicitly incorporated within the solution. The pressure evolves in a way that satisfies the homogeneous Neumann boundary condition automatically, and as a result, the velocity and pressure are updated in the same way as previously discussed in Chapter 2.

The modified governing equations are solved using SIMPLE approach [43], the semi-discrete form of governing equations with IB capability are,

$$\frac{3\mathbf{u}^*}{2\Delta t} + \boldsymbol{L}(\mathbf{u}^*) - \boldsymbol{R}(F^K_{\vec{U^*}}) = \frac{4\mathbf{u}^n - \mathbf{u}^{n-1}}{2\Delta t} + \boldsymbol{N}(\mathbf{u}^n, q^{n+1}, \phi^{n+1}, \theta^{n+1}) \tag{3.9a}$$

$$\boldsymbol{I}(\mathbf{u}^*) = \mathbf{u}^\Gamma(X^K) \tag{3.9b}$$

$$\Delta(\delta p) = \frac{3}{2\Delta t}\nabla \cdot \mathbf{u}^* \tag{3.10}$$

$$\mathbf{u}^{n+1} = \mathbf{u}^* - \frac{2\Delta t}{3}\nabla(\delta p), \quad p^{n+1} = p^n + \delta p \tag{3.11}$$

Also, the energy, charge density, and electric potential equation (3.3-3.5) are rewritten as:

$$\boldsymbol{L}(\phi^{n+1}) - \boldsymbol{R}(F^K_\Phi) = -C \cdot q^n \tag{3.12a}$$

$$\boldsymbol{I}(\phi^{n+1}) = \Phi^\Gamma(X^K) \tag{3.12b}$$

$$\frac{3q^{n+1}}{2\Delta t} - \hat{D}\boldsymbol{L}(q^{n+1}) - \boldsymbol{R}(F_Q^K) = \frac{4q^n - q^{n-1}}{2\Delta t} + \boldsymbol{N}(\phi^{n+1}, \mathbf{u}^n) \tag{3.13a}$$

$$\boldsymbol{I}(q^{n+1}) = Q^\Gamma(X^K) \tag{3.13b}$$

$$\frac{3\theta^{n+1}}{2\Delta t} + \frac{1}{Pr}\boldsymbol{L}(\theta^{n+1}) - \boldsymbol{R}(F_\Theta^K) = \frac{4\phi^n - \phi^{n-1}}{2\Delta t} + \boldsymbol{N}(\theta^n, \mathbf{u}^n) \tag{3.14a}$$

$$\boldsymbol{I}(\theta^{n+1}) = \Theta^\Gamma(X^K) \tag{3.14b}$$

where $\boldsymbol{L}$ refers to the linear term of Laplace operator, $\boldsymbol{I}$ is the linear operator of interpolation and $\boldsymbol{R}$ denotes the regularization. $\boldsymbol{N}$ include all the nonlinear terms explicitly taken from the previous time step n. The Eqns. 3.12b, 3.13b, 3.14b and 3.9b are added to enforce all the given value of field $\Psi^\Gamma(X^K)$ on the Lagrangian points X^K.

3.3.1 Schur complement decomposition

The discrete form of governing equations written in a block-matrix form,

$$\begin{bmatrix} \boldsymbol{H} & \boldsymbol{R} \\ \boldsymbol{I} & 0 \end{bmatrix} \begin{bmatrix} \psi \\ \boldsymbol{F_\Psi} \end{bmatrix} = \begin{bmatrix} RHS_\psi^{n-1,n} \\ \Psi^\Gamma \end{bmatrix} \tag{3.15}$$

where $\boldsymbol{H} = \boldsymbol{L} - \frac{3}{2\Delta t}\mathbf{I}$ for Eqns. 3.13-3.9, and $\boldsymbol{H} = \boldsymbol{L}$ for Eqn. 3.12, are the Helmholtz and the Laplace operators, respectively acting on each component of the predicted vector $\mathbf{u}^*$ and the scalar fields (q, ϕ, θ). $\mathbf{I}$ is the unity matrix, $\boldsymbol{R}$ and $\boldsymbol{I}$ are rectangular matrices that contain terms resulting from applying regularization and interpolation operators, respectively, and $RHS_\psi^{n-1,n}$ stands for the right-hand side vector containing all the other terms left from the original equation (3.12-3.9) known from the previous time steps.

Utilizing the Schur complement approach [48], the system of Eqn. 3.15 is analytically

split into two smaller equivalent systems:

$$\boldsymbol{F}_{\Psi} = [\boldsymbol{I}\boldsymbol{H}^{-1}\boldsymbol{R}]^{-1}[\boldsymbol{I}\boldsymbol{H}^{-1}RHS_{\psi}^{n-1,n} - \Psi^{\Gamma}] \tag{3.16a}$$

$$\psi = \boldsymbol{H}^{-1}[RHS_{\psi}^{n-1,n} - \boldsymbol{R}\boldsymbol{F}_{\Psi}] \tag{3.16b}$$

solution of which is first performed for the distributed Lagrange multiplier terms $\boldsymbol{F}_{\Psi}$ (3.16a), and then for the corresponding Eulerian fields ψ (3.16b). Note that, despite the fact that the process is separated into two stages, the obtained $\boldsymbol{F}_{\Psi}$ and ψ values are fully coupled, as the solution procedure is implicit.

3.3.2 Pseudo time for potential field

Obtaining the solution of the whole problem by a straightforward solution of Eqns. 3.16a and 3.16b would require us to perform inversion of the matrix $[\boldsymbol{I}\boldsymbol{H}^{-1}\boldsymbol{R}]$ typically replaced by LU decomposition. Unfortunately, when dealing with Eqs. 3.12a and 3.12b the Helmholtz operator H should be replaced by the Laplace oeprator, L resulting in a ill-conditioned matrix $[\boldsymbol{I}\boldsymbol{L}^{-1}\boldsymbol{R}]$. An examination of the memory required to perform a LU factorization of the matrix $[\boldsymbol{I}\boldsymbol{L}^{-1}\boldsymbol{R}]$ compared to its $[\boldsymbol{I}\boldsymbol{H}^{-1}\boldsymbol{R}]$ counterpart shows that it takes about 20 times as much memory to calculate the LU decomposition.
Applying a pseudo-time technique allows to decrese the memory consumption and to perform the calculations on grids with high resolution. The key idea is to introduce an additional time dependant parameter ϕ and to perform series of calculations by reducing the value of ϕ at each iteration. The iterations are repeated until the steady state solution of the originial problem is obtained with the required degree of accuracy.

$$\frac{\phi^{k+1}}{\Delta t} + \boldsymbol{L}(\phi^{k+1}) - \boldsymbol{R}(F_{\Phi}^{K}) = \frac{\phi^{k}}{\Delta t} - C \cdot q^{n} \tag{3.17a}$$

$$\boldsymbol{I}(\phi^{k+1}) = \Phi^{\Gamma}(X^{K}) \tag{3.17b}$$

where ^{k} and $^{k+1}$ is the internal iteration index. At every time step, the internal iterations will continue until ϕ^{k+1} and ϕ^{k} become close to each other up to a given precision. Then the simulation proceeds to the next time step by assigning $\phi^{n+1} = \phi^{k+1}$.

3.4 Verification study

The verify the developed thermo hydrodynamic solver, we applied it to the simulation of the electric charge and potential distributions developing between two concentric spheres. This 1D problem has a semi-analytical solution which was first calculated by a specfically written script in Matlab and then compared with the results obtained by the developed IB solver. Two concentric spheres of diameter R_1 and R_2 are placed in the center of cubic enclosure. The numerical-analytical solution is obtained using spherical coordinates. There is no need to solve the Navier-Stokes equations since no electro-thermal convection takes place. Additionally, the solution is 1D in a radial ideraction as it does not depend on the of azimuthal and polar angles. These assumptions are valid when the electric Rayleigh number is low enough to preclude convection. Under these conditions, the transport of free charges is governed solely by migration due to the electric field and molecular diffusion.

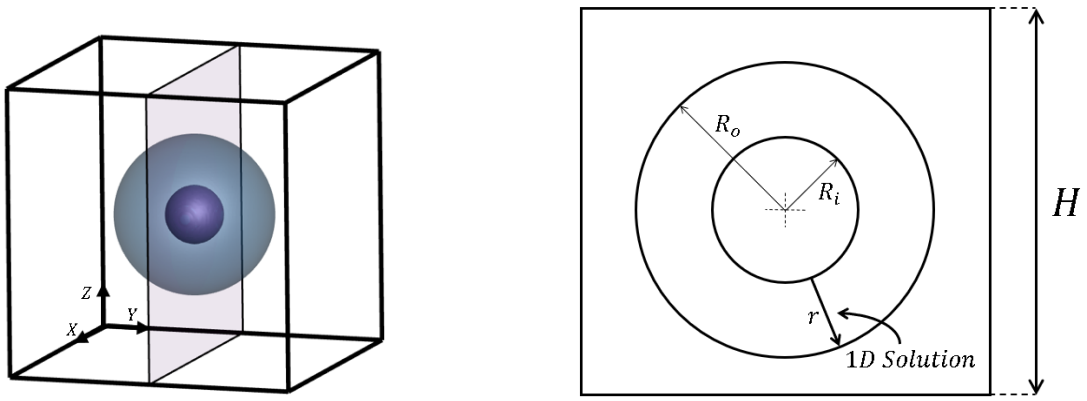

(a) (b)

Figure 3.2: Schematic diagram of two concentric spheres in cube (a) and (b) represents the 2D cross section in the 1D semi-analytical solution along the r direction.

The objective of the simulation is to assess the accuracy and reliability of the solver by simulating the electric charge transport between two concentric spheres. Following the formalism of immersed boundary method the spheres are placed in the center of a cube of length 1 as shown in Figure 3.2. The analysis is performed for the whole 3D domain, although the domain of interest is restricted to the space confined by the two concentric spheres. The inner and the outer spheres have radiuses equal to 0.1 and 0.4, respectively. To ensure the well posed problem, we employed appropriate boundary

conditions on inner and outer surface of sphere (Inner sphere ($r = R_i$) : $\phi = 1 \quad ; \quad q = 2 \quad ; \quad \vec{U} = [0, 0, 0]$, Outer sphere ($r = R_o$) : $\phi = 0 \quad ; \quad q = 1 \quad ; \quad \vec{U} = [0, 0, 0]$).

The computational domain is discretized using a uniform mesh with a resolution of $\Delta x = \Delta y = \Delta z$ and computation are carried out at $M = 49$ and $\hat{D} = 5 \times 10^{-4}$. The properties chosen correspond to silicone oil, used as a working liquid in many experimental studies [23,49]. The simulations are carried with a constant injection field C=10 and varying value of the electric Rayleigh number ($T = 50, 25$ and 10) . The constant injection field ensures a strong injection and viewed as a good approximation of the so-named Space-Charge-Limited (SCL) injection, which can be experimentally achieved by covering the electrode with membrane [50]. The chosen above range of the electric Rayleigh number T values ensures an existence of the underlimiting charge transport for the given configuration.

With the above assumptions the governing equations read as:

$$\nabla^2 \phi = -C \cdot q, \tag{3.18a}$$

$$\nabla \cdot (-\frac{T}{M^2} q \nabla \phi - \hat{D} \nabla q) = 0, \tag{3.18b}$$

Using the product rule to arrange Eqn. 3.18b:

$$\nabla^2 q = \frac{T}{\hat{D} M^2} (C q^2 - \nabla \phi \cdot \nabla q). \tag{3.19}$$

Eqns. 3.18 (a) and 3.19 can be rewritten in spherical coordinates for one-dimensional axi-symmetric confifiguration:

$$\frac{\partial}{\partial r}(r^2 \frac{\partial \phi}{\partial r}) = -r^2 C q, \tag{3.20a}$$

$$\frac{\partial}{\partial r}(r^2 \frac{\partial q}{\partial r}) = r^2 \frac{T}{M^2} \Big[C q^2 - \frac{\partial \phi}{\partial r} \frac{\partial q}{\partial r} \Big] \tag{3.20b}$$

Since the system of equations 3.20 is not linear, the internal iterations are intro-

duced to sove it numerically. The system was solved in a segregated manner by first solving for the Poisson equation 3.20(a) for the electric potential field by taking the charge density field from the previous iteration. The calculated potential field was next plugged into the tarnsport equation for the concentration field. The process has been reiterated until convergence of both fields was achieved with a given precision. The discretization was carried out by utilizing the second order finite difference method. Underrelaxation of both fields was employed to provide a robust convergence of the iterations.

The contours of charge density distribtion in cross section between the spheres, obtained by numerical solution of the fully 3D problem are shown in Figure 3.3 for the value of $T = 50$. As expected the obtained distribution is 1D and varies only in a radial direction. We have cerified that the maximal velue of the flow velocity magnitude was below $O(10^{-4})$, which sucessfully verifies an assumtion of negligible impact of electro-convection in the overall charge space transport for the given configuration.

The space charge distribution obtained by the 3D code has been compared with its counterpart obtained by the solution of axi-symmetric PNP equations for different T values. It can be seen that there is a good agreement between both results, while for the given configuration a grid independance between the 3D results was achieved for 300^3 grids. For this reason all the simutaions performed in the framework of the current study were performed on 300^3 grids.

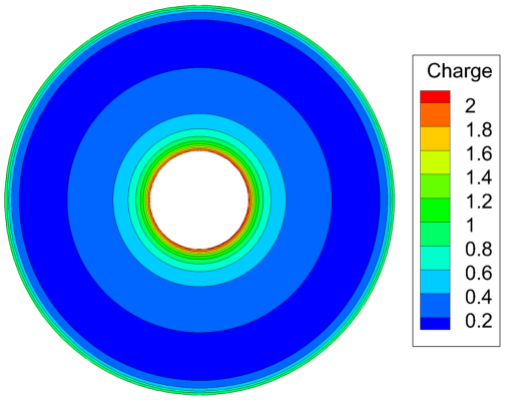

Figure 3.3: Contours of charge density distribution between two concentric spheres.

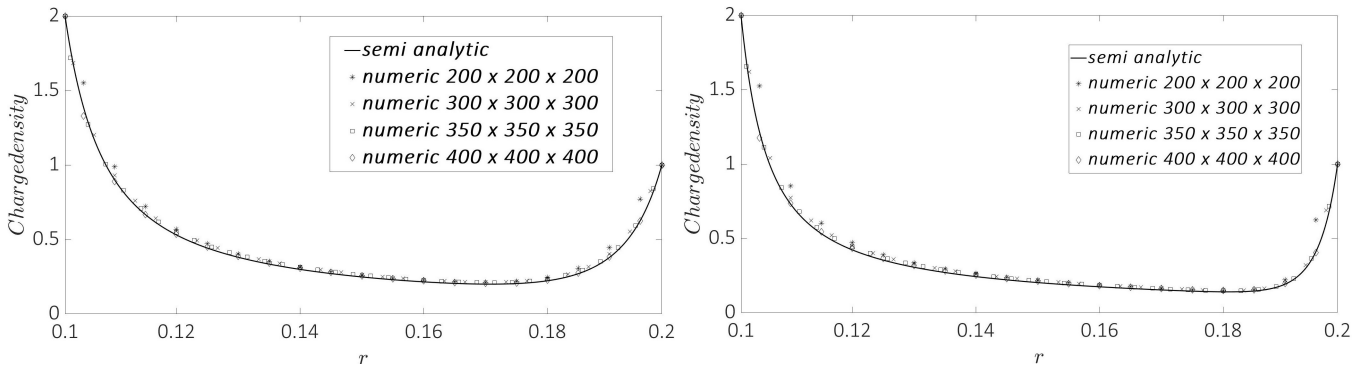

(a) $T = 10$ (b) $T = 25$

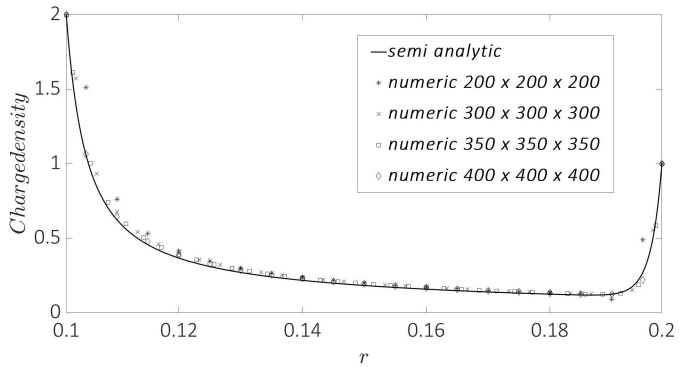

(c) $T = 50$

Figure 3.4: Comparison between the charge density distribution along the radial direction with analytical solution at different electric Rayleigh number (T).

CHAPTER 4

RESULTS AND DISCUSSIONS

In this Chapter, we focus on a set of test problems that involve three-dimensional incompressible electro-thermo-hydrodynamics flows to demonstrate the effectiveness of our direct forcing immersed boundary finite volume framework. Numerical investigations are carried out for pure electro-convection and electro-thermo-convection in cubic enclosures with stationary sphere, placed within the enclosure. The results of electro-convection simulations show symmetry breaking when the electric Rayleigh number is above the value of $T = 900$. Moreover, the electro-thermo-convection flows exhibit unsteady regime for electric Rayleigh number lying in the range between $T = 600$ to $T = 700$. It is important to note that there are no test cases for stationary bodies in the considered electro-thermo-hydrodynamics regimes available in the literature, which makes it challenging to compare our solver with existing literature. However, for stationary body problems, we verify our results against an semi-analytical solution in the previous Chapter 3. It is remarkable that currently conducted simulations demonstrate the ability of the developed approach to accurately handle fully 3D electro-thermo-hydrodynamics flows developing around immersed objects.

4.1 Electro-convection

We commence our analysis by exploring both steady and unsteady electro-convection flows in cube enclosures using the IB-FV solver. The simulations are performed within a square cube with side equal to unity hosting a circular sphere of diameter 0.4 is placed in the center of the cubic enclosure (see Figure 4.1). A no-slip boundary conditions are imposed for all the velocity components on all six wall surfaces of the cube. We consider a uniform grid of resolution $\Delta x = \Delta y = \Delta z = \frac{1}{300}$. All the computations are carried out at $Pr = 116.6$, $M = 49$ and $\hat{D} = 5 \times 10^{-4}$. Following the work of [50], the value of injection strength is equal to $C = 10$. The time steps lie in the range of $10^{-6} <= \Delta t <= 10^{-4}$ and depend on the value of the electric Rayleigh number T. A constant value of electric potential field ($\phi = 1$) is applied on the surface of sphere while all six wall surfaces of the cube are held at $\phi = 0$ value. Assuming that a steady electrochemical reaction takes place between the sphere's surface and the liquid, a homogeneous charge density of value $q = 1$ is applied on the sphere surface. Zero gradient boundary conditiion is applied to the charge density field on all the cavity walls, constituting an open electrode.

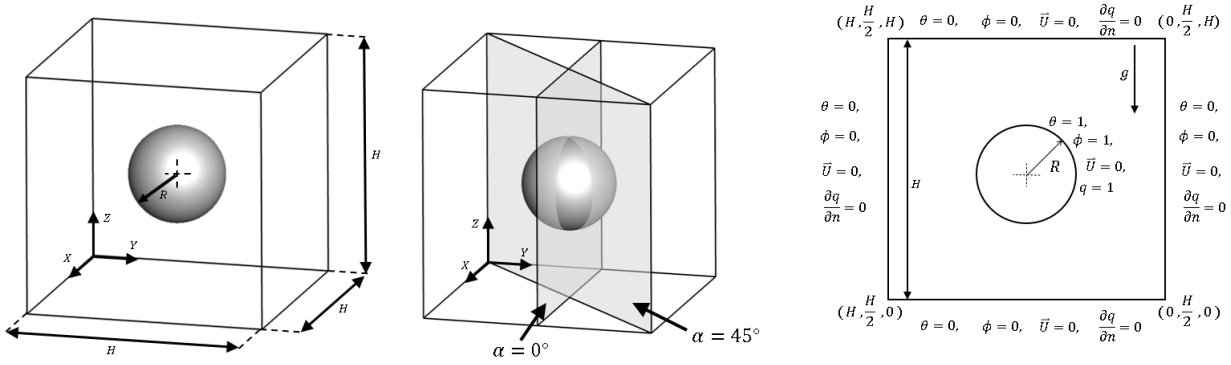

(a) (b) (c)

Figure 4.1: (a) Schematic diagram of a square cube enclosure (b) plane definition of three dimensional computational domain (c) the detailed BCs in the plane $\alpha = 0°$.

The vortical structures of electro-convection are visualized by utilising λ_2 criterion based on the second largest eigenvalue λ_2 of the velocity gradient tensor as discussed in [51]. The λ_2 criterion states that points in a fluid flow where the second largest eigenvalue of the velocity gradient tensor is negative indicate the presence of vortices. After

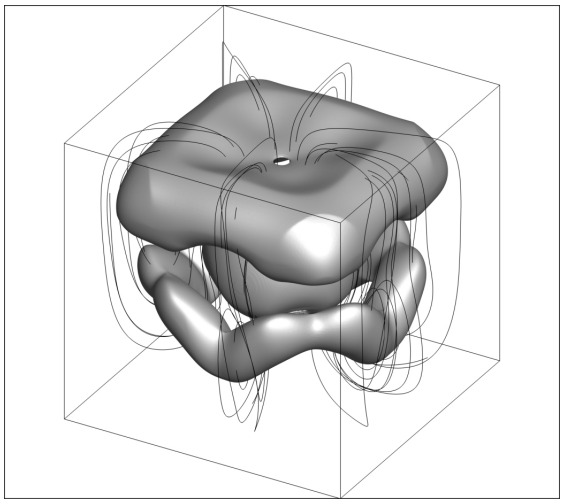

Figure 4.2: Illustrating the relationship between the streamlines and the vortical structures to λ_2 criterion.

a parametric study, a value of $\lambda_2 = -10$ was chosen for the visualization of convection cells. Figure 4.2 shows the relationship between the streamlines and the iso-surface of $\lambda_2 = -10$. The convergence criterion for the steady state simulations performed in the current study was the value of 10^{-6} of L_2 norm calculated for the difference between two consecutive time steps for all the flow fields. Unsteady simulations are continued until the maximum number of time steps is reached.

Seven distinct test cases are chosen to simulate electro-convection problems over a range of electric Rayleigh numbers, starting from the small values and increasing to the larger ones. The steady-state solutions are observed for the range of electric Rayleigh number $T \in [100 - 800]$, while the values of T lying in the range of $T \in [800 - 900]$ characterize non-statiory flow regimes. The steady state flows are investigated in terms of distribution of the charge density and pathlines, projected on the cross-sectional and diagonal midplanes as well as by the iso-surfaces of λ_2 criterion. The charge density distribution shown in Figure 4.3(a-c) is characterized by the the mid crossectional symmetry which indicates that in the steady state regime there is no preffered dirrection in the ionnic transport driven by the drift mechanism of the electric field.

It should be noted that for small value of electric Rayleigh number, $100 \leq T \leq 300$ viscous force dominates the Colombian force governing electro-convection phe-

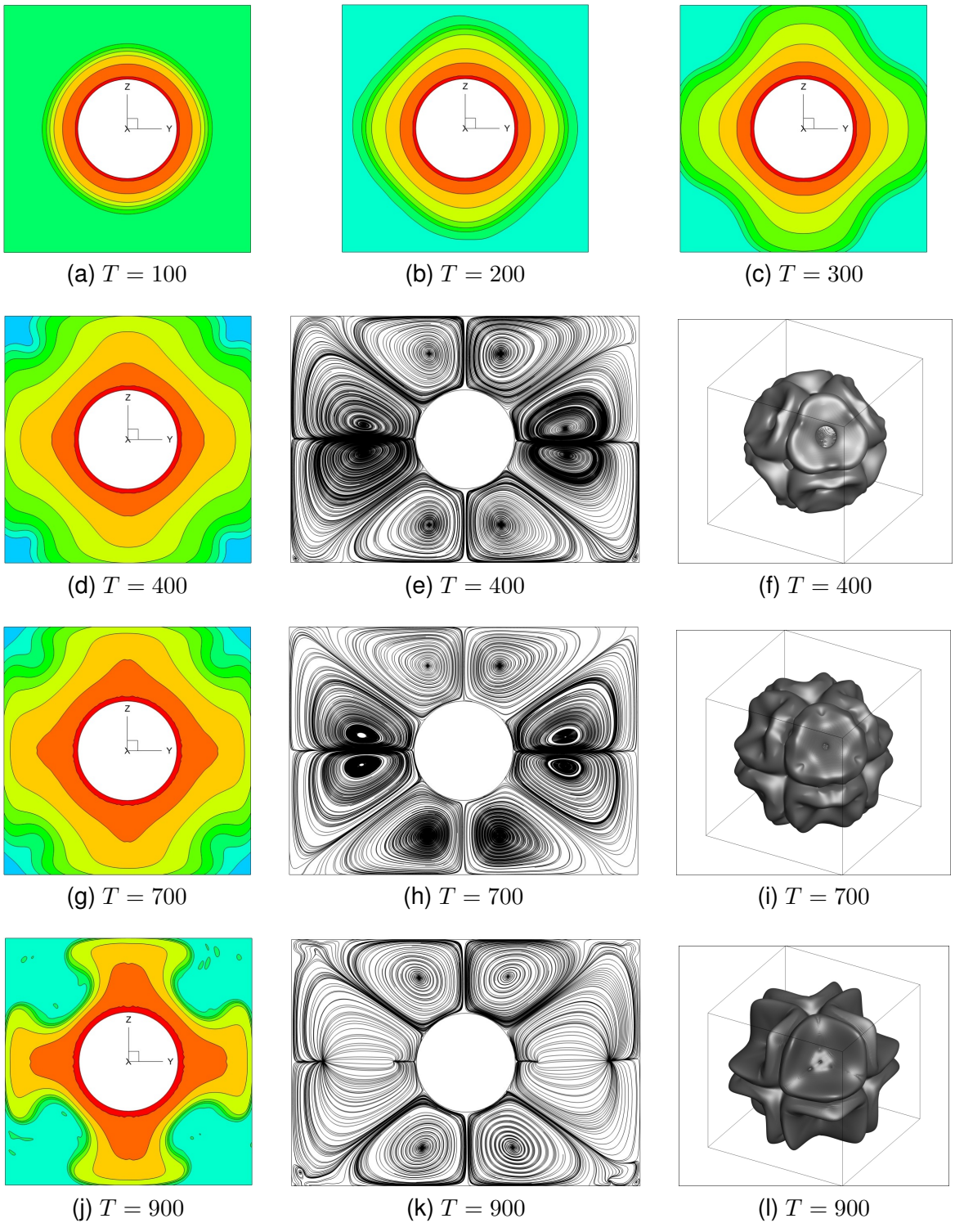

(a) $T = 100$ (b) $T = 200$ (c) $T = 300$

(d) $T = 400$ (e) $T = 400$ (f) $T = 400$

(g) $T = 700$ (h) $T = 700$ (i) $T = 700$

(j) $T = 900$ (k) $T = 900$ (l) $T = 900$

Figure 4.3: (a-c) Show distributions of charge density on $\alpha = 90°$ plane for pseudo conduction regime. Charge density distribution (left), streamlines surface projection (middle), and Iso-surfaces of the $\lambda_2 = -10$ (right) of pure electro-convection. The left and the middle columns correspond to the plane characterized by $\alpha = 90°$ and $\alpha = 45°$ respectively.

nonomenon. As a result, the values of the velocity magnitude are low and convective cells cannot be clearly recognized for this range of T.

The steady state flow obtained for $T = 400$ value preserves mid crossectional symmetry and exhibits eight pairs of counter-rotating vortices as demonstrated in Figure 4.3 (e). It is characterized by four central regions where close to zero values of q are observed as a result of local ballance between the viscous and the electric forces typical of in these regions, see e.g. [52,53]. We also remark that Coulomb-driven flows has a characteristic feature of charge void regime when the Colombian and viscous forces have a same order of magnitude. The qualitative trend of charge void phenomenon is also observed in literature for simulating two dimensional symmetrically-placed electrodes in the domain.

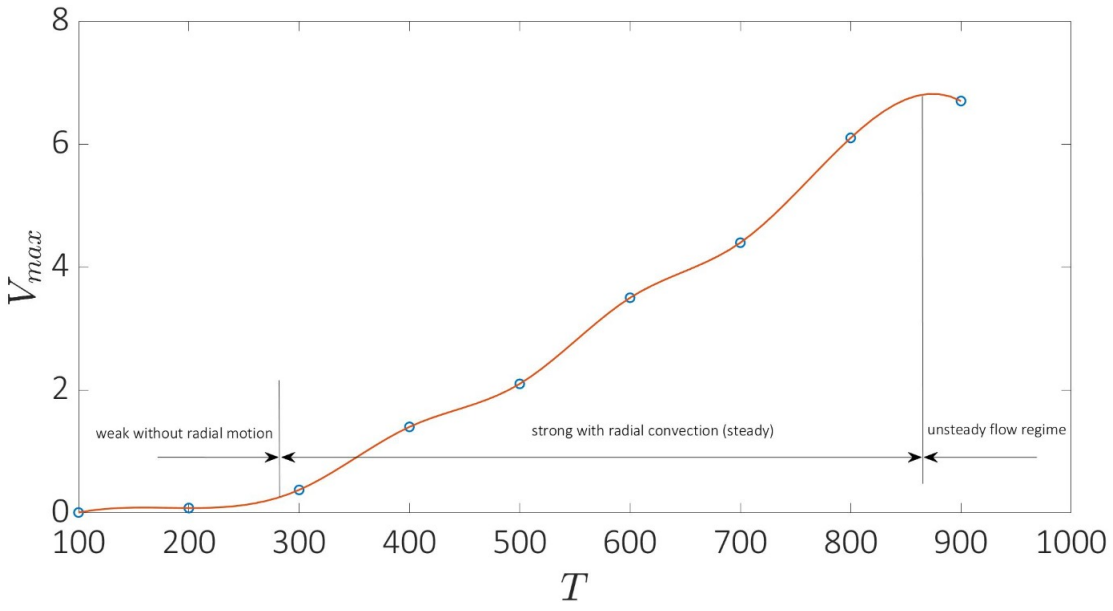

Figure 4.4: The variation of the V_{max} as a function of the electric Rayleigh number T for pure electro-convection.

We next investigate the regimes typical of higher electric Rayleigh number $T \leq 700$ for which the symmetry breaking phenomenon of the electro-convective flow can be clearly recognized. Figure 4.3 (j) also shows thinner charge plumes, which are primarily due to the increased electric force in the domain. It is worth noting that the flow convection mechanism governs the ion transport in the domain since the drift velocity of ions is smaller than the flow velocity, as evidenced in Figure 4.4. Hence,

almost all ions tend to adhere to the regions characterized by the highest flow velocity values.

The relationship between the maximum fluid velocity (V_{max}) and the electric Rayleigh number (T) for electro convection shown in Figure 4.4 reveals two regions distinguishing between the charge density transport regimes with respect to the value of T. The first region is observed between $200 < T < 300$ which leads to a charge void regime while the second region lies in the range of $800 < T < 900$ corresponding to unsteady regime of the electro-convective flow.

It should be noted that for small values of T corresponding to the first regime, the flow strength is not zero, albeit weak. This behavior contrasts the configurations hosting symmetrically placed electrodes; the flow remains at rest. It can be seen that from Figure 4.4 that the transition process is smooth due to the intermediate pattern appearance, and clearly indicates enhancing heat transfer due to electric field.

4.2 Electro-thermo-convection

Now, we focus on the studies of electro-thermo-convection flow where the sphere surface kept at hot constant temperature, $\theta_h = 1$ is placed in the center of a cold cubic enclosure whose all walls are held at cold constant temperatue, $\theta_c = 0$. The analysis requires solution of the energy equation in addition to the Nerns-Planck and electrostatic equations which were addressed in the previous Chapter. The computational domain and simulation parameters are the same with these defined in the previous Section. The thermo-convection is sumulated for a Rayleigh number value equal to $Ra = 10^5$. A series of numerical simulations are performed for the range of electric Rayleigh number $0 \leq T \leq 1300$. The contours of charge and temperature distributions are shown in Figures (4.5,4.6) on plane for $\alpha = 0^\circ, 45^\circ, 90^\circ$. It can be seen that steady state solution obtained for up to $T = 600$ preserves mid plane cross-sectional symmetry while at the higher values of the electric Rayleigh number the symmetry breaking phenomenon can be clearly recognized both in electric charge and temperature distribution as ahown in Figure 4.6.

The vortical structure of electro-thermo-convection exhibits a variety of different behaviors with respect to different values of the electric Rayleigh number as depicted in a Figures (4.8-4.7). For close to zero values of the electric Rayleigh number the effects of electric field forces on the fluid are negligible leading to pure thermal convection regime as shown in Figure 4.8(a) wihle the vortical structure shows a typical for the natural convetion flows mushroom-shaped structure.

Further increasing of the electric Rayleigh number to the value of $T = 100$, does not lead to significant changes in the flow which is still dominated by the buoyancty forces and charcterized by the clearly recognized thermal plume adjacent to the top wall of the cube (see Fig. 4.5 (b)). Similiarly to the purely convective flow $(T = 0)$ the flow developing at $T = 100$ is also characterized by a mushroom shaped vortical structure. As the electric Rayleigh number is increased to 200, the electric force becomes strong enough to induce the formation of two additional convective cells , whose size tends to grow with increasing T up to $T = 500$ value. As the Rayleigh number is increased above 300, the electric force becomes strong enough to distort the mushroom-shaped vortical structure and form convective cells of more comlex shapes, as shown in Figure 4.7 (d-g).

As the Rayleigh number is increased to above $T = 600$, the electric forces becomes strong enough to dominate the flow and induce the formation of more than two additional convection rolls, as shown in Figure 4.8. These rolls can interact with each other and give rise to complex flow patterns, such as secondary flows and instabilities, which can lead to asymmetries in the charge and temperature distributions as well as in the vortical structure of the domain. At higher values of the electric Rayleigh number, the vortical structure of electro-thermo-convection can become highly turbulent and exhibit a wide range of scales, from large-scale rolls to small-scale eddies. In this regime, the flow patterns can be highly irregular and difficult to predict, and may display features such as intermittent bursts of activity, chaotic behavior, and the formation of localized regions with high vorticity and mixing. A thorough investigation of the above flow features remained out of the scope of the current study.

4.3 Heat flux calculation

The Nusselt number is defined as a ratio of convective to conductive heat fluxes. In our study, the averaged Nusselt number on the surface of the cube refers as $\overline{Nu_c}$ and $\overline{Nu_h}$ denotes the averaged Nusselt number on the surface of the sphere. The surface-averaged Nusselt number on the cube faces is defined as:

$$\overline{Nu_c} = \frac{1}{N}\sum_{i=1}^{N}\overline{\frac{\partial\theta}{\partial \boldsymbol{n}}}, \tag{4.1}$$

where $\overline{\frac{\partial\theta}{\partial \boldsymbol{n}}}$ refers to the averaged temperature gradient on the surface of given faces of the cubic enclosure, and N is the number of thermally conducting faces. The energy equation is typically solved using the direct forcing immersed boundary (IB) method, which does not involve a sharp demarcation of the boundary surface within the region. As a result, the solid boundary does not conform to the Cartesian mesh underlying the computational domain and edges of the solid are not readily available for calculation of the average heat fluxes. The averaged Nusselt number on the spheres is calculated as:

$$\overline{Nu_h} = Pr\Delta x\overline{f_\theta}, \tag{4.2}$$

Where $\overline{f_\theta}$ is the average heat flux obtained by an arithmetic mean of all the non-dimensional heat fluxes f_θ^K at each Lagrangian point X^k of the immersed surface.
At steady state, the value of the total dimensionless heat flux entering into system from the sphere should be the same as that leaving the cube. The total averaged flux is calculated by multiplying it by the total area of the cube faces. For the steady state solution, the following condition should satisfy:

$$4\pi R^2\overline{Nu_h} \approx 6H^2\overline{Nu_c}. \tag{4.3}$$

4.4 Heat transfer

This section discusses the enhancement of heat transfer by the Coulomb force. The heat transfer enhancement by electro-convection is analyzed by using the averaged Nusselt numbers $\overline{Nu}_h$ and $\overline{Nu}_c$ as discussed in previous Section.

Figure 4.9 depicts dependance of the Nusselt number averaged over the surface of a sphere, $\overline{Nu}_h$, as a function of the electric Rayleigh number T. As the Coulomb force becomes stronger (with an increase in T), the electric field induces a radial flow, resulting in an increase in convective heat transfer. The results shown in Figure 4.9 can be categorized into two cases. For low T values (ranging from 0 to approximately 250), the heat transfer is dominated by thermal convetction and therefore its variation with T is weak. For higher T values (ranging from 300), the slope of the $\overline{Nu} - T$ curve increases dramatically at about $T = 300$ and remains approximately constant for the higher T values.

It is interestibg to compare the above $\overline{Nu} - T$ dependance obtained for fully 3D flow with the results previously obtained for 2D configurations and available in the literature. To perform the above comparison we focus on the work of [15] who ibvestigated both natural and electroconvection flows developing in 2D cold square container with hot circular cylinder placed in the center of the container. The length of the box side and the diameter of the cylinder are the same as in the length of the cube side and the diameter of the sphere used in the current study.

In contrast to the $\overline{Nu} - T$ curve currently obtained for 3D configuration, the curve obtained for 2D flow is characterized by clearly recognizible transition region separating betwen the thermally and the electrically dominated regimes as shown in Fig. 4.10 (adapted from [15]). This behavior can be explained by the fact that the 2D flow is chrarcterzed by a critical threshold value of T above which electro-convection solely controls the flow structure, and the impact of the buoyancy forces becomes negligible. In the simulation conducted in this work, full dominance of electro-convection is not achieved even at very high T values (up to 1300). At the same time the flow pattern structure obtained for high values of T qualitatively resembles its 2D counterpart.

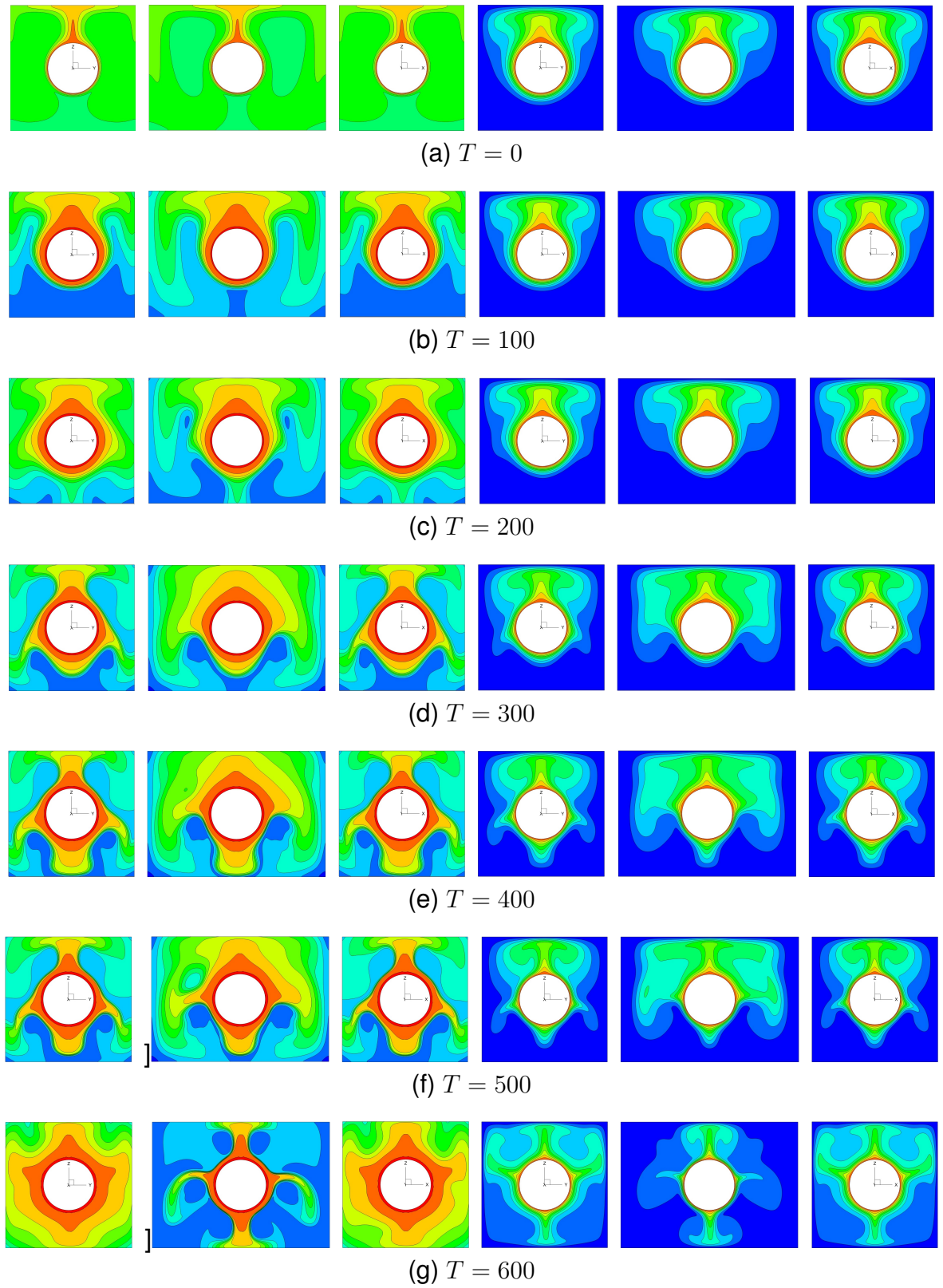

(a) $T = 0$

(b) $T = 100$

(c) $T = 200$

(d) $T = 300$

(e) $T = 400$

(f) $T = 500$

(g) $T = 600$

Figure 4.5: Charge density (left) and temperature distribution (right) for electro-thermo-convection with $Ra = 10^5$ and different values of T. The planes characterized by $\alpha = 0°, 45°, 90°$ from left to right respectively

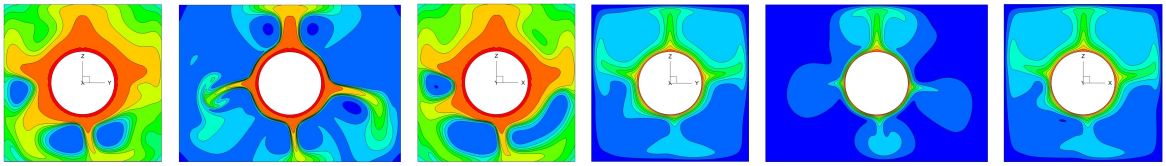

(a) $T = 700$

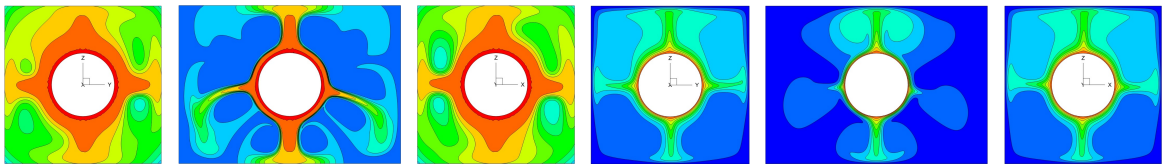

(b) $T = 800$

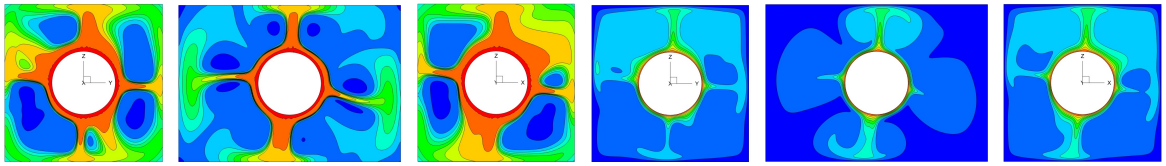

(c) $T = 900$

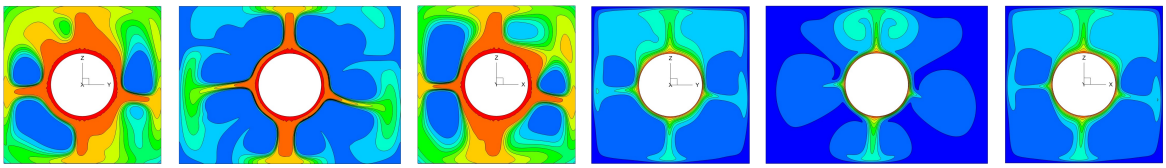

(d) $T = 1000$

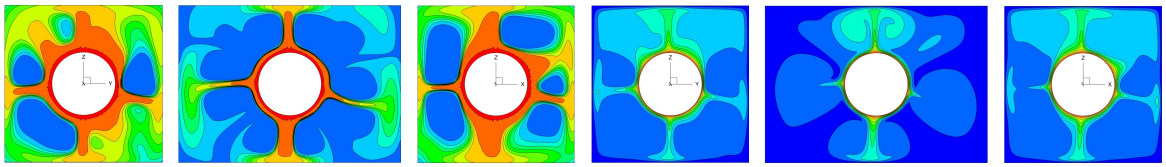

(e) $T = 1100$

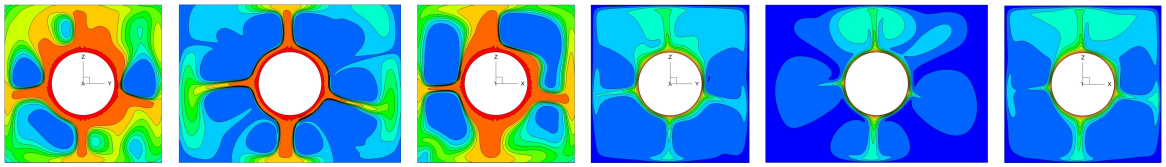

(f) $T = 1200$

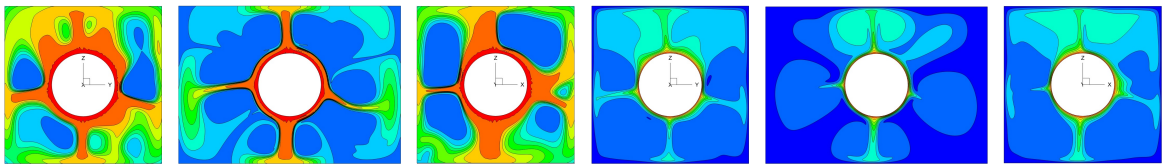

(g) $T = 1300$

Figure 4.6: Charge density (left) and temperature distribution (right) for electro-thermo-convection with $Ra = 10^5$ and different values of T. The planes characterized by $\alpha = 0°, 45°, 90°$ from left to right respectively

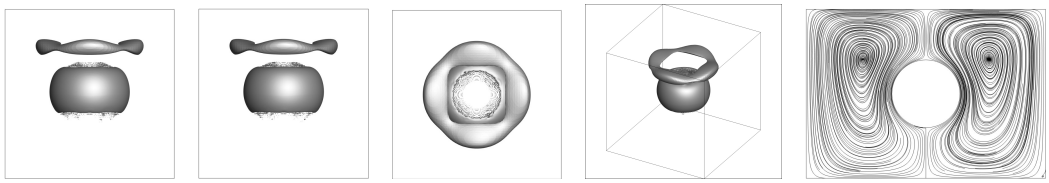

(a)$T = 0$

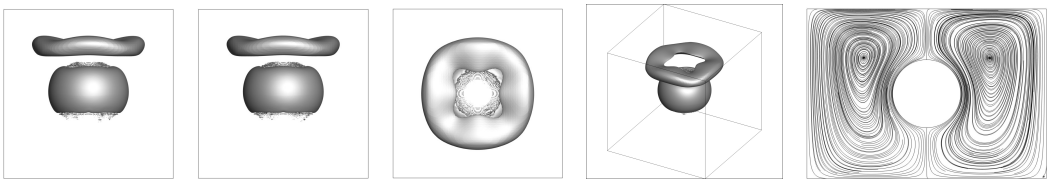

(b)$T = 100$

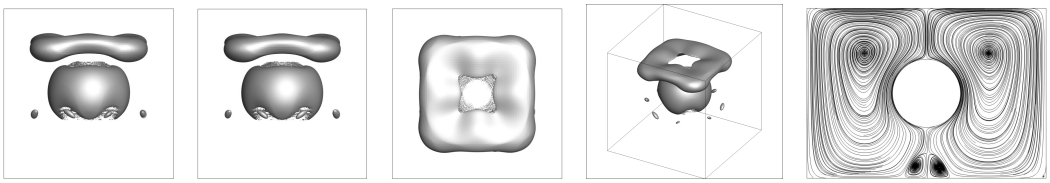

(c)$T = 200$

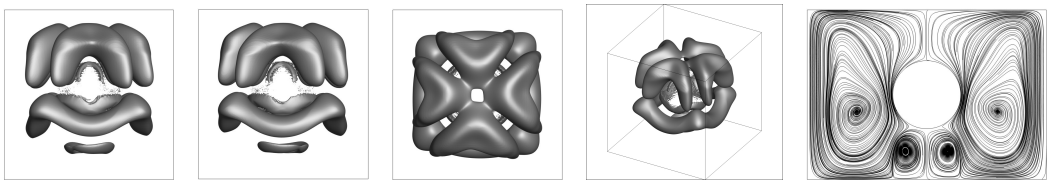

(d)$T = 300$

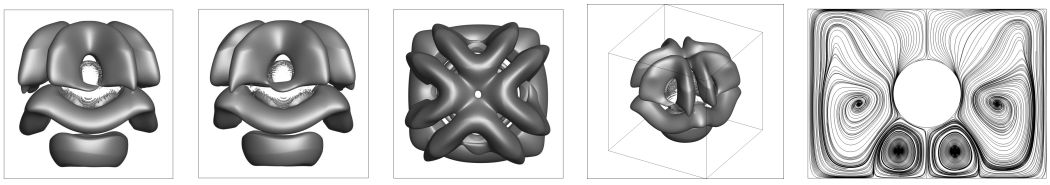

(e)$T = 400$

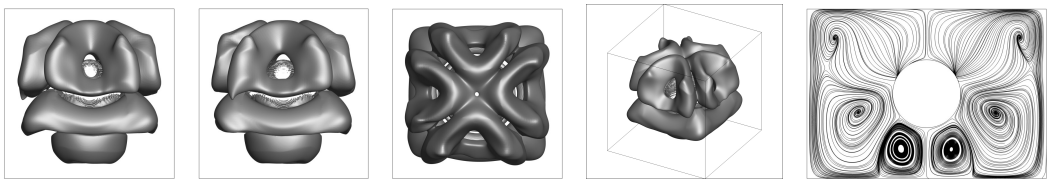

(f)$T = 500$

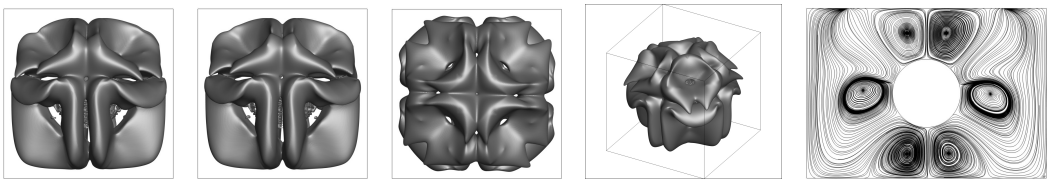

(g)$T = 600$

Figure 4.7: Vortical structure using $\lambda_2 = -10$ at $Ra = 10^5$ and different values of T, from left to right corresponds to the Z-Y, Z-X, X-Y planes, isometric view and the sreamline at planes $\alpha = 45$, respectively.

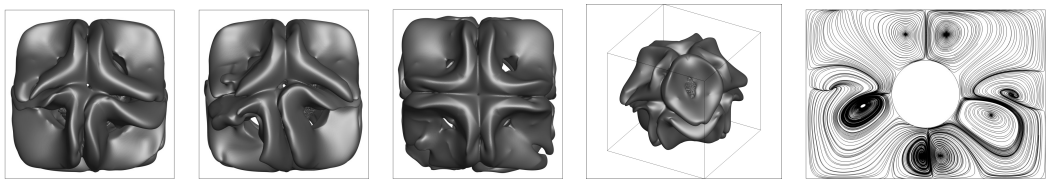

(a)$T = 700$

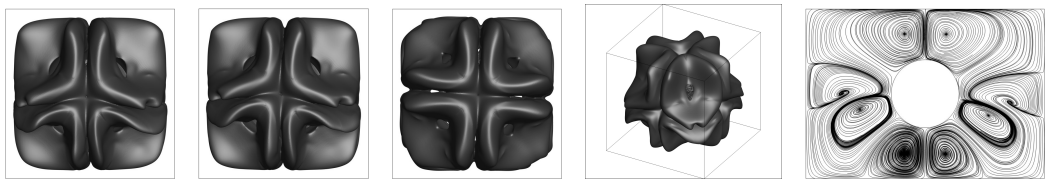

(b)$T = 800$

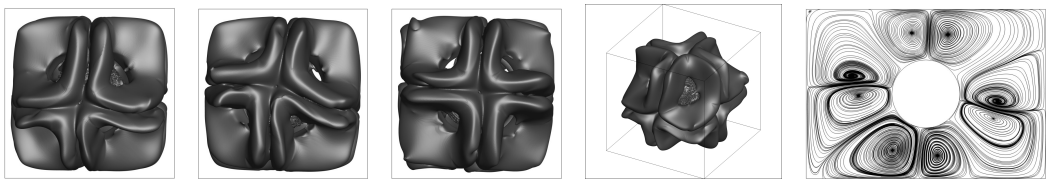

(c)$T = 900$

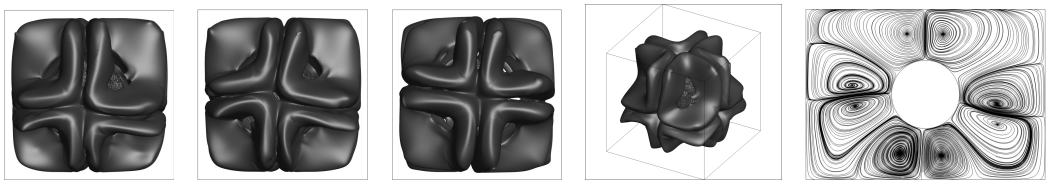

(d)$T = 1000$

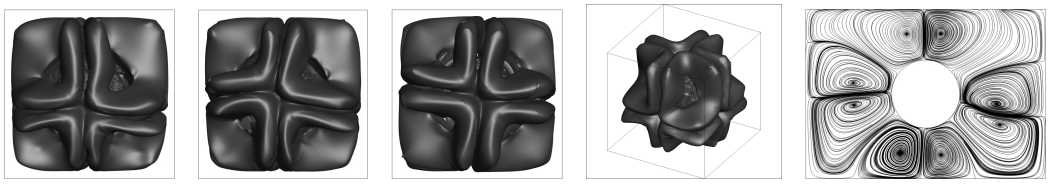

(e)$T = 1100$

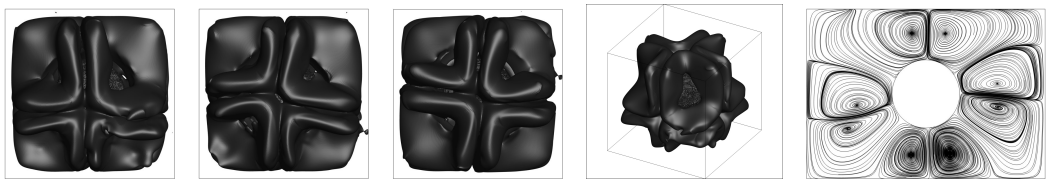

(f)$T = 1200$

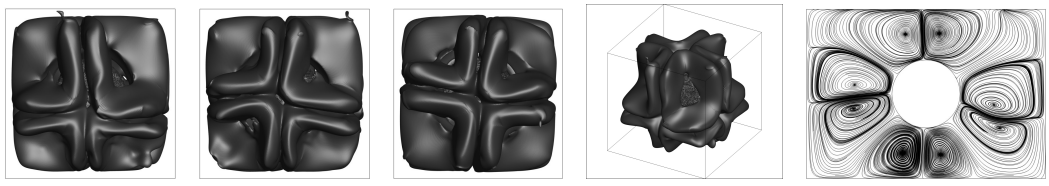

(g)$T = 1300$

Figure 4.8: Vortical structure using $\lambda_2 = -10$ at $Ra = 10^5$ and different values of T, from left to right corresponds to the Z-Y, Z-X, X-Y planes, isometric view and the sreamline at planes $\alpha = 45$, respectively

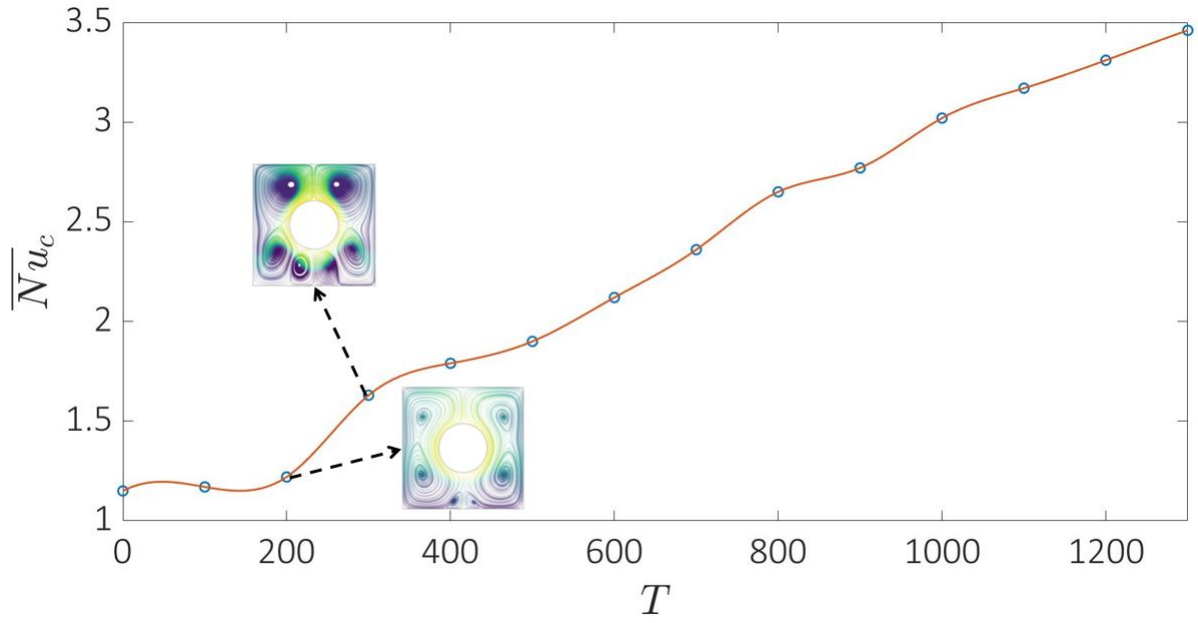

Figure 4.9: The averaged Nusselt number variation on the surface of cubic enclosures at the different value of electric Rayleigh number T.

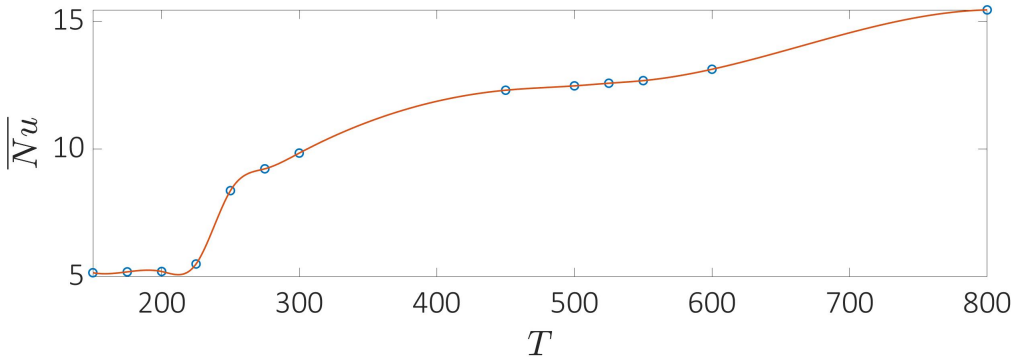

Figure 4.10: The averaged Nusselt number variation on the surface of a hot inner cylinder for two-dimensional cylinder placed in a cubic configuration at the different value of electric Rayleigh number T [15].

CHAPTER 5

SUMMARY AND CONCLUSIONS

This chapter provides a summary of the main characteristics of the direct forcing immersed boundary/finite volume framework proposed in this thesis for the simulation of electro-thermo-hydrodynamic flows. We emphasize the key contributions, highlight notable observations and offer suggestions for future research directions.

The focus of the thesis was the extension of a direct forcing immersed boundary finite volume solver for electro-thermo-hydrodynamics, with a view to handling bodies of complex geometry. We have employed finite volume method on a staggered grid that is capable of handling electro-thermo-convection in enclosure. A large spectrum of test problems involving electro-convection and electro-thermo-convection in enclosures have been considered to assess the IB-FV framework proposed in the thesis. The salient conclusions on the developed framework and subsequent numerical investigations are enumerated below.

1. The framework developed in this study has been proven for its capability to accurately simulate electro-thermo-convection flows. The momentum equation is solved at the cell faces, while the charge, energy, and pressure equations are solved at the cell centroid. To enable the use of the direct solver MUMPS with limited memory resources, the pseudo-time technique was employed in the stationary Poisson equation. This technique reduced the RAM requirement for com-

putations by nearly 20 times.

2. The thesis proposes a novel approach for simulating electro-thermo-hydrodynamics flows using a direct forcing immersed boundary (IB) method. The resulting IB-FV solver is accurate and capable of handling one or more bodies. The developed solver was favorably verified by applying it to a simplified electro-fluid flow problem and comparing the outcomes with a one-dimensional semi-analytical solution. The three-dimensional problem was simulated under conditions of sub convection (T low enough) between two concentric spheres, preserving a spherical symmetry. A comparison between the one-dimensional and the comprehensive three-dimensional solutions was performed by employing interpolation of the corresponding fields along the radial axis.

3. The Numerical simulation results were presented for the electro-convection of and thermal convection in a cubic enclosure. The flow structures of pure thermal convection and electro-convection differ from each other due to the different directions of the buoyant and Coulomb forces and the different transport mechanisms in the motionless state.

4. Finally, the proposed IB-FV solver for electro-thermo-convection problem was investigated to understand the influence of the Coulomb forces on the flow hydrodynamics. It was found that the heat flux is strongly effected by electric field and charge injection, as after the electric driving parameter T exceeded a critical threshold. This strong dependance is attributed to the appearance of radial convection induced by the Coulomb force. It should be noted that the prediction of an exact value of T at which the flow convection sets on in radial direction remained out of the scope of the current study. Rather, we focused on determining the range of T values at which the transition takes place.

5. Future work can focus on performing a parametric study of the different physical and geometrical parameters and their influence on the flow regimes and the heat transfer enhancement. The parameters whose influence can be analyzed are, for example, the liquid properties ($Pr, M,$ and D), the applied operating conditions (Ra and C), and the geometrical characteristics (such as Γ).

REFERENCES

[1] H. E. Ahmed, M. I. Ahmed, Thermal performance of annulus with its applications; a review, Renewable and Sustainable Energy Reviews 71 (2017) 170–190.

[2] J. Sun, L. Zhang, Z. Li, Q. Tang, J. Chen, Y. Huang, C. Hu, H. Guo, Y. Peng, Z. L. Wang, A mobile and self-powered micro-flow pump based on triboelectricity driven electroosmosis, Advanced Materials 33 (34) (2021) 2102765.

[3] S.-I. Jeong, J. Seyed-Yagoobi, Experimental study of electrohydrodynamic pumping through conduction phenomenon, Journal of Electrostatics 56 (2) (2002) 123–133.

[4] A. Ratzabi, T. Eluk, A. Levy, Y. Feldman, Nonsymmetric ionic transport in a nonbinary electrolyte at high voltage, Physical Review Fluids 6 (11) (2021) 113701.

[5] S. Chakraborty, S. Das, Streaming-field-induced convective transport and its influence on the electroviscous effects in narrow fluidic confinement beyond the debye-hückel limit, Physical Review E 77 (3) (2008) 037303.

[6] T. B. Jones, Electrohydrodynamically enhanced heat transfer in liquids—a review, Advances in heat transfer 14 (1979) 107–148.

[7] S. Laohalertdecha, P. Naphon, S. Wongwises, A review of electrohydrodynamic enhancement of heat transfer, Renewable and Sustainable Energy Reviews 11 (5) (2007) 858–876.

[8] L. Léal, M. Miscevic, P. Lavieille, M. Amokrane, F. Pigache, F. Topin, B. Nogarède, L. Tadrist, An overview of heat transfer enhancement methods and new perspectives: Focus on active methods using electroactive materials, International Journal of heat and mass transfer 61 (2013) 505–524.

[9] W. Grassi, D. Testi, Heat transfer enhancement by electric fields in several heat exchange regimes, Annals of the New York Academy of Sciences 1077 (1) (2006) 527–569.

[10] C. M. Rhie, W.-L. Chow, Numerical study of the turbulent flow past an airfoil with trailing edge separation, AIAA journal 21 (11) (1983) 1525–1532.

[11] R. Mittal, G. Iaccarino, Immersed boundary methods, Annu. Rev. Fluid Mech. 37 (2005) 239–261.

[12] Y. Feldman, Semi-implicit direct forcing immersed boundary method for incompressible viscous thermal flow problems: a schur complement approach, International Journal of Heat and Mass Transfer 127 (2018) 1267–1283.

[13] H. Bénard, Les tourbillons cellulaires dans une nappe liquide.-méthodes optiques d'observation et d'enregistrement, Journal de Physique Théorique et Appliquée 10 (1) (1901) 254–266.

[14] L. Rayleigh, Lix. on convection currents in a horizontal layer of fluid, when the higher temperature is on the under side, The London, Edinburgh, and Dublin Philosophical Magazine and Journal of Science 32 (192) (1916) 529–546.

[15] K. Luo, J. Wu, H.-L. Yi, H.-P. Tan, Numerical investigation of heat transfer enhancement in electro-thermo-convection in a square enclosure with an inner circular cylinder, International Journal of Heat and Mass Transfer 113 (2017) 1070–1085.

[16] A. Castellanos, Electrohydrodynamics, Vol. 380, Springer Science & Business Media, 1998.

[17] G. Ahsmann, R. Kronig, The influence of electric fields on the convective heat transfer in liquids, Applied Scientific Research 2 (1) (1951) 235–244.

[18] H. De Haan, The influence of electric fields on the convective heat transfer in liquids ii, Applied Scientific Research, Section A 3 (1) (1951) 85–88.

[19] H. Senftleben, W. Braun, Der einfluss elektrischer felder auf den wärmestrom in gasen, Zeitschrift für Physik 102 (7-8) (1936) 480–506.

[20] P. Traore, A. Pérez, D. Koulova, H. Romat, Numerical modelling of finite-amplitude electro-thermo-convection in a dielectric liquid layer subjected to both unipolar injection and temperature gradient, Journal of Fluid Mechanics 658 (2010) 279–293.

[21] K. Dantchi, T. Philippe, R. Hubert, W. Jian, L. Christophe, Numerical simulations of electro-thermo-convection and heat transfer in 2d cavity, Journal of Electrostatics 71 (3) (2013) 341–344.

[22] J. Wu, P. Traoré, A finite-volume method for electro-thermoconvective phenomena in a plane layer of dielectric liquid, Numerical Heat Transfer, Part A: Applications 68 (5) (2015) 471–500.

[23] P. Atten, F. McCluskey, A. Perez, Electroconvection and its effect on heat transfer, IEEE Transactions on Electrical Insulation 23 (4) (1988) 659–667.

[24] P. Martin, A. Richardson, Overstable electrothermal instabilities in a plane layer of dielectric liquid, Journal of Electrostatics 12 (1982) 435–439.

[25] Q. Wang, Y. Guan, T. Wei, J. Wu, Transition sequences and heat transfer enhancement in electro-thermo-convection of a dielectric liquid between two parallel electrodes, International Journal of Thermal Sciences 179 (2022) 107705.

[26] W. Worraker, A. Richardson, The effect of temperature-induced variations in charge carrier mobility on a stationary electrohydrodynamic instability, Journal of Fluid Mechanics 93 (1) (1979) 29–45.

[27] W. Nernst, Die elektromotorische wirksamkeit der jonen, Zeitschrift für physikalische Chemie 4 (1) (1889) 129–181.

[28] M. Planck, Ueber die erregung von electricität und wärme in electrolyten, Annalen der Physik 275 (2) (1890) 161–186.

[29] L. Boltzmann, Studien uber das gleichgewicht der lebenden kraft, Wissenschafiliche Abhandlungen 1 (1868) 49–96.

[30] P. Debye, E. Hückel, De la theorie des electrolytes. i. abaissement du point de congelation et phenomenes associes, Physikalische Zeitschrift 24 (9) (1923) 185–206.

[31] C. S. Peskin, Flow patterns around heart valves: a numerical method, Journal of computational physics 10 (2) (1972) 252–271.

[32] C. S. Peskin, The immersed boundary method, Acta numerica 11 (2002) 479–517.

[33] X. Yang, X. Zhang, Z. Li, G.-W. He, A smoothing technique for discrete delta functions with application to immersed boundary method in moving boundary simulations, Journal of Computational Physics 228 (20) (2009) 7821–7836.

[34] H. Yoon, D. Yu, M. Ha, Y. Park, Three-dimensional natural convection in an enclosure with a sphere at different vertical locations, International Journal of Heat and Mass Transfer 53 (15-16) (2010) 3143–3155.

[35] W. Ren, C. Shu, J. Wu, W. Yang, Boundary condition-enforced immersed boundary method for thermal flow problems with dirichlet temperature condition and its applications, Computers & Fluids 57 (2012) 40–51.

[36] W. Ren, C. Shu, W. Yang, An efficient immersed boundary method for thermal flow problems with heat flux boundary conditions, International Journal of Heat and Mass Transfer 64 (2013) 694–705.

[37] Y. Gulberg, Y. Feldman, On laminar natural convection inside multi-layered spherical shells, International Journal of Heat and Mass Transfer 91 (2015) 908–921.

[38] Y.-H. Tseng, J. H. Ferziger, A ghost-cell immersed boundary method for flow in complex geometry, Journal of computational physics 192 (2) (2003) 593–623.

[39] J. Shao, C. Shu, Y.-T. Chew, Development of an immersed boundary-phase field-lattice boltzmann method for neumann boundary condition to study contact line dynamics, Journal of Computational Physics 234 (2013) 8–32.

[40] Y. Hu, D. Li, X. Niu, S. Shu, An immersed boundary-lattice boltzmann method for electro-thermo-convection in complex geometries, International Journal of Thermal Sciences 140 (2019) 280–297.

[41] B. Kim, D. Lee, M. Ha, H. Yoon, A numerical study of natural convection in a square enclosure with a circular cylinder at different vertical locations, International journal of heat and mass transfer 51 (7-8) (2008) 1888–1906.

[42] C.-C. Liao, C.-A. Lin, Influences of a confined elliptic cylinder at different aspect ratios and inclinations on the laminar natural and mixed convection flows, International Journal of Heat and Mass Transfer 55 (23-24) (2012) 6638–6650.

[43] S. V. Patankar, D. B. Spalding, A calculation procedure for heat, mass and momentum transfer in three-dimensional parabolic flows, in: Numerical prediction of flow, heat transfer, turbulence and combustion, Elsevier, 1983, pp. 54–73.

[44] A. M. Roma, C. S. Peskin, M. J. Berger, An adaptive version of the immersed boundary method, Journal of computational physics 153 (2) (1999) 509–534.

[45] Y. G. Park, M. Y. Ha, C. Choi, J. Park, Natural convection in a square enclosure with two inner circular cylinders positioned at different vertical locations, International Journal of Heat and Mass Transfer 77 (2014) 501–518.

[46] D. B. Stein, R. D. Guy, B. Thomases, Immersed boundary smooth extension (ibse): a high-order method for solving incompressible flows in arbitrary smooth domains, Journal of Computational Physics 335 (2017) 155–178.

[47] T. Kempe, J. Fröhlich, An improved immersed boundary method with direct forcing for the simulation of particle laden flows, Journal of Computational Physics 231 (9) (2012) 3663–3684.

[48] E. V. Haynsworth, On the schur complement., Tech. rep., BASEL UNIV (SWITZERLAND) MATHEMATICS INST (1968).

[49] F. McCluskey, P. Atten, A. Perez, Heat transfer enhancement by electroconvection resulting from an injected space charge between parallel plates, International journal of heat and mass transfer 34 (9) (1991) 2237–2250.

[50] J. Lacroix, P. Atten, E. Hopfinger, Electro-convection in a dielectric liquid layer subjected to unipolar injection, Journal of Fluid Mechanics 69 (3) (1975) 539–563.

[51] J. Jeong, F. Hussain, On the identification of a vortex, Journal of fluid mechanics 285 (1995) 69–94.

[52] K. Luo, J. Wu, H.-L. Yi, H.-P. Tan, Lattice boltzmann model for coulomb-driven flows in dielectric liquids, Physical Review E 93 (2) (2016) 023309.

[53] N. Felici, J. Lacroix, Electroconvection in insulating liquids with special reference to uni-and bi-polar injection: a review of the research work at the cnrs laboratory for electrostatics, grenoble 1969–1976, Journal of Electrostatics 5 (1978) 135–144.

תקציר

עבודת גמר זו מציגה את פיתוח מתודולוגית "immersed boundary (IB)" מורחבת בדיסקריטיזציית נפחים סופיים (finite volume - FV) עבור זרימות אלקטרו-הידרודינמיות עם מעבר חום.
המשוואות השולטות עוברות דיסקריטיזציה באמצעות שיטת נפחים סופיים על רשת קרטזית מדורגת.
הפותרן שפותח מיישם שיטת נפחים סופיים ושיטת הפרשים סופיים אחוריים מסדר שני לדיסקרטיזציה במרחב ובזמן, בהתאמה.
פותרן הנפח הסופי משמש כבסיס להטמעת טכניקות ה IB המוצעות בתזה.
התזה מציעה גישת IB באכיפה ישירה עבור זרימות אלקטרו-הידרודינמיות עם מעבר חום.
גישה זו מניחה שפונקציית האכיפה מתווספת למשוואות Navier-Stokes ושאר המשוואות השימור, מה שמאפשר בנייה של משוואות שולטות מתוקנות המתייחסות לתנאי הגבול של Dirichlet ו-Neumann כאחד.
הדיוק של פותרן IB-FV נבדק עבור זרימות אלקטרו-הידרודינמיות, ונמצא שהוא מספק בדיוק הנדרש.
הפותרן מסוגל לחשב את מספר Nusselt הממוצע על פני השטח בדיוק גבוה באמצעות שימוש במקורות החום המובנים בשיטת ה.IB
הרעיון העומד בבסיס שיטת הIB באכיפה ישירה המוצגת בעבודה זו הוא להרחיב את מנעד הפתרונות האפשריים באמצעות הפותרן גם לבעיות אלקטרו-תרמו-הסעה.
הפותרן המתקבל מסוגל להתמודד עם בעיות אלקטרו-תרמו-הסעה המתפתחות סביב גופים שקועים בעלי גיאומטריה שרירותית.
סדרת מקרי בוחן מייצגים שבוצעו במסגרת עבודה זו מדגימים את הדיוק והיעילות של פותרן ה-IB-FV לזרימות אלקטרו-הידרודינמיות עם העברת חום.
מקרי הבוחן הרבים המוצגים בתזה זו משמשים להערכה מקיפה ולביסוסה של שיטת הIB-FV המוצעת בעלת האכיפה ישירה כגישה אמינה, פשוטה ומדויקת להדמיית זרימות אלקטרו-הידרודינמיות עם מעבר חום.
מקרי בוחן אלו מדגימים את יעילותה של השיטה המוצעת בהדמיית סוגים שונים של זרימות, כולל זרימות אלקטרו-הסעה ואלקטרו-תרמו-הסעה, ואת יכולתה לחשב במדויק את מספר Nusselt הממוצע על פני השטח ואת מבנה הערבולים המדויק המתקבל. התוצאות מצביעות על כך שהשיטה המוצעת היא כלי חישובי אמין ויעיל לחקר זרימות אלקטרו-הידרודינמיקה עם מעבר חום.
כהיבט חדשני, הפותרן שפותח נוצל לחקר הפוטנציאל של זרימה המושרה על ידי כוח חשמלי בשיפור קצב העברת החום מכדור עם הזרקת מטען מפני השטח השקוע בנוזל מבודד לחלוטין.

אוניברסיטת בן־גוריון בנגב
הפקולטה למדעי ההנדסה
המחלקה להנדסת מכונות

פיתוח מטודולוגיה נומרית להדמיה תלת מימדית של זרימה אלקטרו תרמית בטווח תחום

חיבור זה מהווה חלק מהדרישות לקבלת התואר מוסמך בהנדסה (M.Sc)

יוחאי מעין

בהנחיית **ד"ר יורי פלדמן**

חתימת המחבר: _____ תאריך: 21.03.2023

אישור המנחים: _____ תאריך: 21.03.2023

אישור יו"ר ועדת תואר שני מחלקתית: _____ תאריך: 21/3/23

ד"ר בני בר-און
יו"ר לימודי מוסמכים
המחלקה להנדסת מכונות

מרץ 2023

אוניברסיטת בן־גוריון בנגב
הפקולטה למדעי ההנדסה
המחלקה להנדסת מכונות

פיתוח מטודולוגיה נומרית להדמיה תלת מימדית של זרימה אלקטרו תרמית בטווח תחום

חיבור זה מהווה חלק מהדרישות לקבלת התואר מוסמך למדעי הטבע (M.Sc)

יוחאי מעין

בהנחיית **ד"ר יורי פלדמן**

מרץ 2023